



JWST: Deuterated PAHs, PAH Nitriles, and PAH Overtone and Combination Bands. I. Program Description and First Look

C. Boersma¹ , L. J. Allamandola¹ , V. J. Esposito¹ , A. Maragkoudakis¹ , J. D. Bregman¹ , P. Temi¹ , T. J. Lee¹ ,
R. C. Fortenberry² , and E. Peeters^{3,4} 

¹NASA Ames Research Center, MS 245-6, Moffett Field, CA 94035-1000, USA; Christiaan.Boersma@nasa.gov

²Department of Chemistry & Biochemistry, University of Mississippi, University, MS 38677-1848, USA

³Department of Physics and Astronomy & The Institute for Earth and Space Exploration, The University of Western Ontario, London, ON N6A 3K7, Canada

⁴Carl Sagan Center, SETI Institute, 189 Bernardo Avenue, Suite 200, Mountain View, CA 94043, USA

Received 2023 June 19; revised 2023 October 6; accepted 2023 October 9; published 2023 December 7

Abstract

A first look is taken at the NIRSpec 1–5 μm observations from James Webb Space Telescope program 1591 that targets seven objects along the low-mass stellar life cycle with polycyclic aromatic hydrocarbon (PAH) emission. Spectra extracted from a 1''5 radius circular aperture are explored, showing a wealth of features, including the 3 μm PAH complex, the PAH continuum, and atomic and molecular emission lines from H I, He, H₂, and other species. CO₂- and H₂O-ice absorption and CO emission is also seen. Focusing on the bright-PDR position in M17, the PAH CH stretch falls at 3.29 μm (FWHM = 0.04 μm). Signs of its 1.68 μm overtone are confused by line emission in all targets. Multicomponent decomposition reveals a possible aliphatic deuterated PAH feature centered at 4.65 μm (FWHM = 0.02 μm), giving $[D/H]_{\text{alip.}} = 31\% \pm 12.7\%$. However, there is little sign of its aromatic counterpart between 4.36 and 4.43 μm . There is also little sign of PAH nitrile emission between 4.34 and 4.39 μm . A PAH continuum rises from ~ 1 to 3.2 μm , after which it jumps by about a factor of 2.5 at 3.6 μm , with bumps at 3.8, 4.04, and 4.34 μm adding structure. The CO₂ absorption band in M17 is matched with 10:1 H₂O:CO₂ ice at 10 K. The $\nu = 0$ pure rotational molecular hydrogen population diagram reveals >2200 K UV-pumped gas. The hydrogen Pfund series runs from levels 10 to >30 . Considering $\text{Br}\alpha/\text{Br}\beta = 0.381 \pm 0.01966$ and Case B recombination results in $A_V \simeq 8$. CO emission in IRAS 21282+5050 originates from 258 K gas. In-depth spectral–spatial analysis of all features and targets is planned for a series of forthcoming papers.

Unified Astronomy Thesaurus concepts: Polycyclic aromatic hydrocarbons (1280); Near infrared astronomy (1093); Interstellar molecules (849); Laboratory astrophysics (2004)

1. Introduction

The James Webb Space Telescope (JWST; Gardner et al. 2023) launched Christmas morning 2021. After a roughly 6 month commissioning period, JWST started science operations. General Observer (GO) Cycle 1 program 1591, titled *NIRSpec IFU: Deuterated PAHs, PAH nitriles, and PAH Overtone and Combination Bands*, obtained its first set of observations in 2022 September and the final set in 2023 May. This paper describes that program and takes a first exploratory look at the data.

The program set out to measure the 1–5 μm spectra of seven objects that represent key stages in the low-mass stellar life cycle and have strong polycyclic aromatic hydrocarbon (PAH) emission. The PAH model predicts many, but weak, features in this region that are able to resolve questions that have faced the PAH model since its inception. While the Infrared Space Observatory (ISO; de Graauw et al. 1996) and Akari (Onaka et al. 2007) have pioneered some of this spectral range, NIRSpec-IFU's (Böker et al. 2022, 2023) sensitivity and spectral resolution make it possible, for the first time, to measure the PAH signature with high fidelity across the entire region.

The goals of the program are to quantify the amount of cosmological deuterium sequestered in PAHs, quantify the

PAH deuterium/hydrogen and carbon/nitrogen ratios, track these ratios through the stellar life cycle, and provide insight into intermediate PAH structures, sizes, and charge states that determine how PAHs grow, erode, and evolve. The unique information contained in the 1–5 μm bands will forward our understanding of the interplay between PAHs and their environment and how they influence that same environment.

This paper is organized as follows. Section 2 describes the observations and details the data reduction. Section 3 presents the results, and Section 4 provides a discussion. The paper finishes with a summary and conclusions in Section 5.

2. Observations

JWST GO Cycle 1 program 1591 targets seven well-studied astronomical PAH sources that cover key stages of the low-mass stellar life cycle. Within the confines of a small, 25 hr program, a careful balance was sought for obtaining a data set that would maximize discovery space, have a guaranteed science return, and not overcommit observing time. Table 1 summarizes the astrometric data of the targets, where it is noted that M17 was observed at two different positions, and IRAS 21292+5050 has a separate, dedicated background observation.

Utilizing the NIRSpec instrument in its IFU mode (Böker et al. 2022, 2023), a total of eight ~ 1 –5 μm medium-resolution ($R \equiv \lambda/\Delta\lambda \simeq 1000$) spatial–spectral observations were obtained, covering a field of view of $\sim 3''7 \times 4''7$ at a pixel size of $0''1 \times 0''1$. All observations use a four-point dither and the G140M/F100LP (0.97–1.89 μm), G235M/F170LP

Table 1
Astrometric and Observational Parameters

Target	R.A. (ICRS)	Decl. (ICRS)	Obs. Date ^a	Type	Groups ^b	LeakCal	Pattern	Exp.
M17-PDR	18 20 23.26	-16 12 31.28	2022 Sep 7	H II	4	x	NRSIRS2	4.45 hr
M17-B-PDR ^c	18 20 24.35	-16 11 52.96	2022 Sep 9	H II	8	x	NRSIRS2	6.22 hr
NGC 1333-SVS3	03 29 10.40	+31 21 51.12	2022 Sep 17	RN	10	...	NRSIRS2RAPID	2.05 hr
NGC 2023-PDR ^d	05 41 41.00	-02 15 41.70	2022 Oct 12	RN	20	x	NRSIRS2RAPID	4.15 hr
NGC 2023-PDR ^e	05 41 41.00	-02 15 41.70	2023 Feb 19	RN	20	x	NRSIRS2RAPID	4.15 hr
IRAS 21282+5050-RIM	21 29 58.69	+21 29 58.69	2022 Sep 16	PPN	10	...	NRSIRS2RAPID	1.42 hr
IRAS 21282+5050-BKG	21 29 57.99	+51 03 50.92	2022 Sep 16	PPN	10	...	NRSIRS2RAPID	1.42 hr
HD 44179-SPIKE ^d	06 19 57.98	-10 38 07.22	2022 Oct 10	PPN	9	...	NRSIRS2RAPID	1.81 hr
HD 44179-SPIKE ^e	06 19 57.98	-10 38 07.22	2023 Feb 19	PPN	9	...	NRSIRS2RAPID	1.81 hr
BD +303639-RIM	19 34 45.28	+30 30 52.72	2022 Sep 20	PN	9	...	NRSIRS2RAPID	1.99 hr
NGC 7027-EDGE	21 07 01.50	+42 14 20.79	2023 May 25	PN	10	...	NRSIRS2RAPID	1.86 hr

Notes.

^a Data are proprietary in MAST for 1 yr after being observed.

^b All observations were taken using a single integration.

^c Originally named M17-MC but adjusted here, as the position clearly probes the bright PDR.

^d Observation affected by a short in the microshutter assembly.

^e Retake of observation affected by a short in the microshutter assembly per Webb Operations Problem Report (WOPR 88608).

(1.66–3.17 μm), and G395M/F290LP (2.87–5.27 μm) grating/filter combinations to cover 1–5 μm . Background (one target) and LeakCal (three targets) observations were limited to only a few targets, and readout patterns were adjusted accordingly. Table 1 also summarizes the observational parameters used for each target.

2.1. Targets

The seven objects targeted are well studied, have PAH emission, and probe different stages along the low-mass stellar life cycle. Each object is briefly discussed below, following the stages along the low-mass stellar life cycle, starting with H II regions.

M17—M17 is located in Sagittarius at a distance of 1800 pc (Kharchenko et al. 2005). It is one of the most massive known nearby star-forming regions (Povich et al. 2009) and is irradiated by seven O stars, the most luminous being the binary system CEN1 with an effective temperature of 41,200 K (Chini et al. 1980).

Figure 1 shows a three-color composite image obtained by the SIRIUS (Nagashima et al. 1999) instrument at the IRSF 1.4 m telescope. Overlaid are a number of telescope apertures, including 10 from ISO-SWS that trace the emission from the H II region, crossing the photodissociation region (PDR) all the way into the molecular region (Verstraete et al. 1996). Also shown are two ISOCAM (Crete et al. 1999) and eight Akari apertures (Doney et al. 2016) that focus on the H II region. The footprint of Spitzer-IRS spectral map observations are shown as four translucent colored patches, where each patch represents a distinct emission zone. These zones were identified through hierarchical clustering on the integrated intensity normalized spectra and reflect changes in the shape of the spectrum (see Boersma et al. 2018).

Two positions were targeted in M17. The first, labeled JWST-PDR, is centered on the location that has a tentative detection of deuterated PAHs (Peeters et al. 2004). The second, labeled JWST-B-PDR, probes the bright PDR.

Dependent on the exact location and employed (emission) model, Peeters et al. (2004) determined an aliphatic-to-aromatic ratio of 0.36 ± 0.08 for this source, while Onaka et al. (2014)

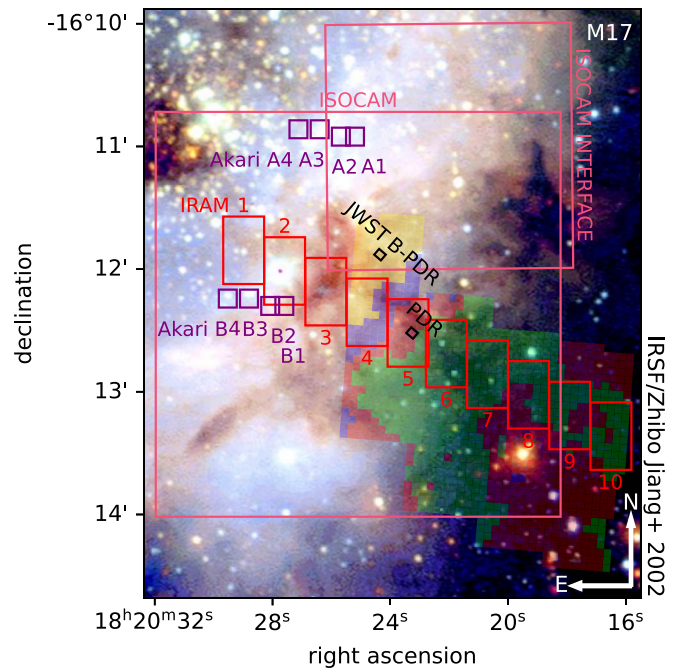


Figure 1. IRSF/SIRIUS three-color composite image of M17, with *J*-band data shown in blue, *H*-band data in green, and *K_s*-band data in red. Image credits: Jiang et al. (2002). Superimposed are telescope/instrument apertures from ISOCAM (pink), ISO-SWS (red), and Akari (purple) observations. The two JWST apertures are shown and labeled in black. The translucent colored patches mark Spitzer-IRS spectral map observations, where each patch represents one of four distinct emission zones identified through hierarchical clustering (see Boersma et al. 2018).

found 0.023 ± 0.004 , and Doney et al. (2016) found 0.09 ± 0.05 .

NGC 1333-SVS3—NGC 1333 is located in Perseus, some 330 pc from Earth (Racine & van den Bergh 1970). SVS3 is the reflection nebula (RN) in NGC 1333 that is illuminated by a likely binary composed of a 15,700 and a 6810 K F2 star (Straizys et al. 2002). Figure 2 presents the morphology of the SVS3 region as seen by the 8.2 m Subaru telescope. Overlaid are a number of telescope apertures, including those from ISOCAM and ISO-SWS observations. Also overlaid, marking

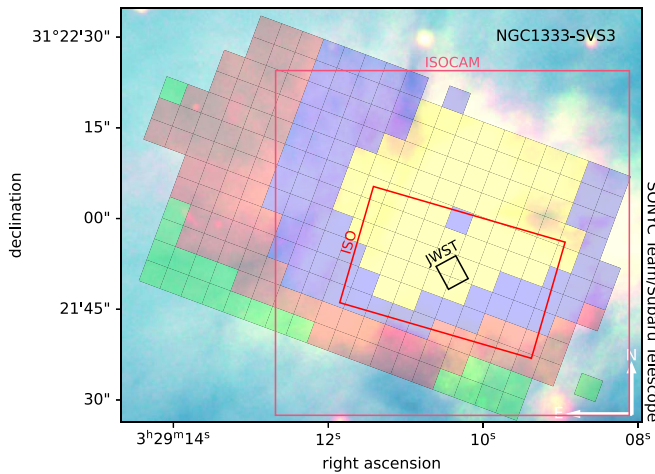


Figure 2. Three-color composite Subaru image of part of NGC 1333-SVS3. Here the blue channel is taken from i' -band, the green from J -band, and the red from K -band data. Image credits: SONYC Team/Subaru Telescope. Superimposed are apertures from ISOCAM (pink) and ISO-SWS (red) observations. The translucent colored patches mark Spitzer-IRS spectral map data, where each color represents one of four zones identified through hierarchical clustering (see Boersma et al. 2016). The JWST aperture is shown and labeled in black.

Spitzer-IRS spectral map observations, are translucent patches indicating four distinct emission zones identified through hierarchical clustering (see Boersma et al. 2016 and the description of M17). It is noted that the available Spitzer spectral map data cover a substantially larger region but were trimmed to only encompass that with strong PAH emission. The targeted JWST borders a nebulous outflow arc that can be seen in ISOCAM imagery.

NGC 1333-SVS3 has been the subject of numerous studies (e.g., Joblin et al. 1996; Sloan et al. 1999; Stock et al. 2016, and references therein). For a review, see Walawender et al. (2008).

NGC 2023—NGC 2023 is the RN located some 415 pc from Earth in Orion (Menten et al. 2007). It hosts a cluster of faint, most likely pre-main-sequence stars, where the radiation environment is dominated by HD 37903, a B1.5 24,800 K star (Mookerjee et al. 2009). Figure 3 presents the morphology of the region as seen by VISTA (Dalton et al. 2006; Emerson et al. 2006). Overlaid are a number of telescope apertures, including those from ISOCAM (Abergel et al. 2001), ISO-SWS (Moutou et al. 1999), and Spitzer (Andrews et al. 2015) single-slit observations. Also overlaid are colored translucent patches marking Spitzer-IRS spectral map observations depicting four emission zones identified through hierarchical clustering (see Boersma et al. 2016 and the description of M17). The JWST position is the brightest spot in the nebula (Peeters et al. 2012).

PAH emission in NGC 2023 has been the subject of numerous studies, including Pilleri et al. (2012), Boersma et al. (2016), Stock et al. (2016), Peeters et al. (2017), Zang et al. (2019), and Sidhu et al. (2021).

IRAS 21282+5050—IRAS 21282+5050 is a young, ~ 3000 yr old, very compact, low-excitation protoplanetary nebula (PPN; Cohen & Jones 1987; Bregman et al. 1992). It is located 4000 pc from Earth (Gaia Collaboration 2020) and hosts both a 28,000 K post-AGB and a 6000 K main-sequence star. Figure 4 shows a three-color composite Hubble image constructed from data obtained from the Hubble Legacy Archive overlaid with the aperture of ISO-SWS observations (Beintema et al. 1996).

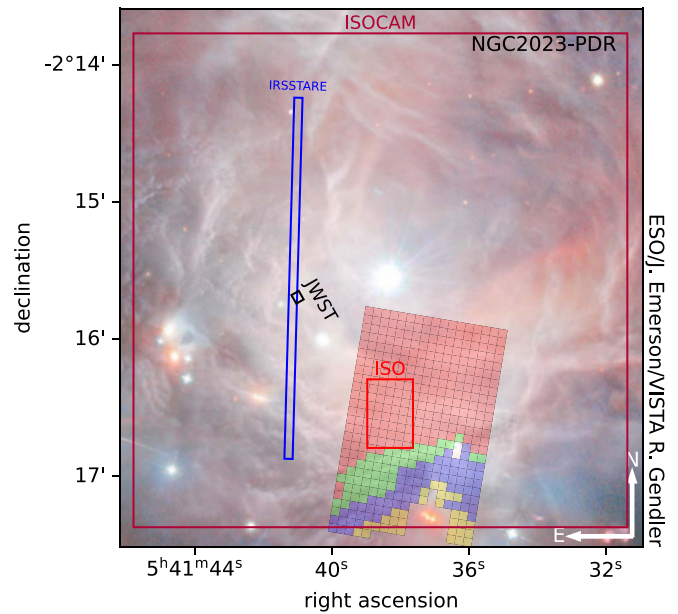


Figure 3. VISTA image of part of NGC 2023. Image credits: ESO/J. Emerson/VISTA R. Gendler. Superimposed are telescope/instrument apertures for ISOCAM (pink), ISO-SWS (red), and Spitzer (blue slit) observations. The colored translucent overlay marks Spitzer-IRS spectral map observations, where each color represents one of four distinct emission zones identified through hierarchical clustering (see Boersma et al. 2016). The JWST aperture is shown and labeled in black.

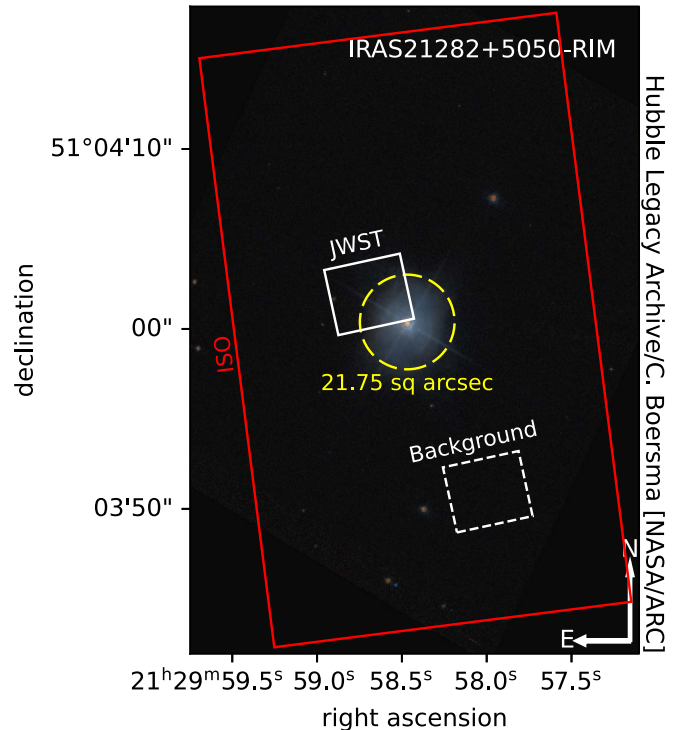


Figure 4. Hubble-ACS three-color composite image of IRAS 21282+5050, with F814W data shown in red, F606W data in blue, and an equal mixture of F814W and F606W data in green. Superimposed is the aperture from ISO-SWS (red) observations, and the apparent size of the nebula is indicated by the yellow dashed circle. The JWST apertures for the science target and separate dedicated background are shown and labeled in white, with the latter dashed.

An aliphatic-to-aromatic band strength ratio of ~ 0.47 has been determined for this source, suggesting early-stage photochemical processing (Hsia et al. 2019; Smith et al. 2020).

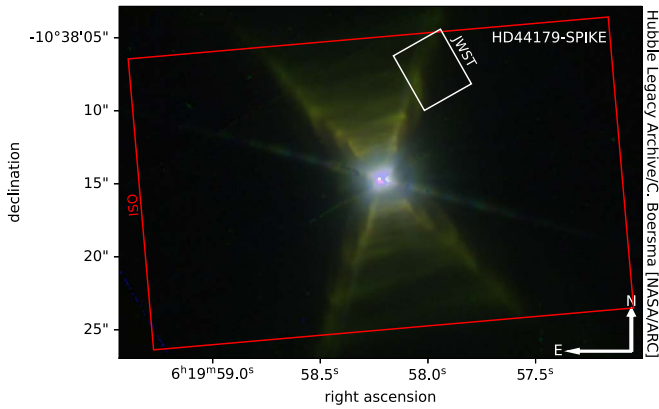


Figure 5. Three-color composite HST WFPC2 image of HD 44179, with the red channel taken from narrowband F631N data tracing [O I], the green channel from narrowband F588N data tracing He I, and the blue channel from medium Strömgren b -band F467M data. Superimposed is the aperture from ISO-SWS (red) observations. The JWST aperture is shown and labeled in white.

In addition, the $\sim 1.67 \mu\text{m}$ overtone of the $3.3 \mu\text{m}$ PAH band has been tentatively detected here (Kwok et al. 1993; Geballe et al. 1994; Chen et al. 2019).

The JWST position borders the outskirts, avoiding the brightest parts of the nebula.

HD 44179 (The Red Rectangle)—HD 44179 is a young, low-excitation PPN with a 23,000 K mass accretion-driven radiation field hosting a 7700 K post-AGB and a < 6000 K main-sequence star (Witt et al. 2009). HD 44179 has a complex geometry with an x-shaped outflow with density enhancements resembling rungs on a ladder.

Figure 5 shows a three-color composite Hubble image constructed from data obtained from the Hubble Legacy Archive overlaid with the aperture of ISO-SWS observations (Waters et al. 1998). The JWST aperture is located on one of the “beams” of the x-shaped ladder, where the ISOCAM spectrum is dominated by PAH emission.

The $3.3 \mu\text{m}$ PAH emission feature in HD 44179 has been of particular interest; it has been suggested to consist of two distinct spectroscopic components (Song et al. 2003, 2007; Candian et al. 2012). However, this has recently been disputed (Tokunaga et al. 2022).

BD +303639—BD +303639 is a very young, ~ 600 yr old, moderate-excitation ($T_{\text{star}} \simeq 47,000$ K) planetary nebula (PN; Siebenmorgen et al. 1994) located 1600 pc from Earth (Gaia Collaboration 2020). An aliphatic/aromatic ratio of ~ 0.24 has been measured (Smith et al. 2020). The faint structure near $3.4 \mu\text{m}$ in its ISO-SWS spectrum suggests that PAH sculpting has started, where the least thermodynamically favored side groups are being removed (Leuenhagen et al. 1996; Smith et al. 2020).

Figure 6 shows the Gemini North adaptive optics image of the nebula. Overlaid are telescope apertures from ISOCAM (Persi et al. 1999) and ISO-SWS (Bernard-Salas et al. 2003) observations. The targeted position is located on the ring, where the ISOCAM spectrum shows strong PAH emission, but avoids the brightest parts of the nebula.

NGC 7027 (Jewel Bug Nebula)—NGC 7027 is a young, ~ 700 yr old, very high excitation ($T_{\text{star}} \simeq 198,000$ K) PN (Cox 1998; Latter et al. 2000) located in Cygnus, some 920 pc from Earth. Figure 7 shows the three-color composite Hubble image constructed from data obtained from the Hubble Legacy Archive overlaid with apertures from ISOCAM (Persi et al. 1999) and ISO-SWS (Beintema et al. 1996) observations. The targeted

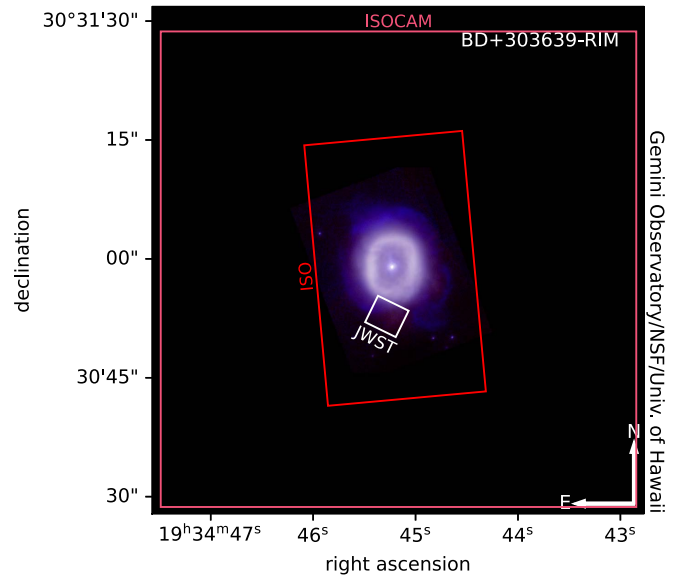


Figure 6. Three-color composite infrared adaptive optics image of BD +303639 from the Gemini North 8 m telescope. The blue and red channels show narrowband H_2 and $\text{Br}\gamma$ emission, respectively. Image credits: Gemini Observatory, US National Science Foundation, and University of Hawaii Institute for Astronomy. Superimposed are apertures from ISOCAM (pink) and ISO-SWS (red) observations. The JWST aperture is shown and labeled in white.

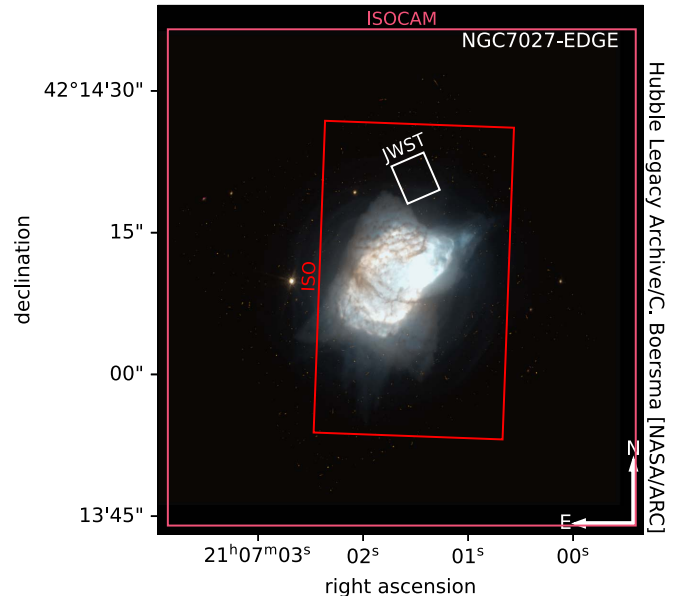


Figure 7. Three-color composite HST image of NGC 7027 with WFPC2 F55W data in red, F814W data in blue, and a combination of the two in green. Superimposed are apertures of ISOCAM (pink) and ISO-SWS (red) observations. The JWST aperture is shown and labeled in white.

JWST position lies on the outskirts of the nebula, where the ISOCAM spectrum shows a relatively moderate amount of PAH emission, and the brightest regions of the nebula are avoided.

2.2. Data Reduction

Level-1b⁵ data associated with JWST program 1591 were downloaded from MAST using the Python *astroquery*

⁵ STScI processed data: [10.17909/x16g-g718](https://doi.org/10.17909/x16g-g718).

package. The JWST Detector1Pipeline was run on the downloaded uncalibrated data using default parameters. Subsequently, association files were generated, ensuring proper tagging of LeakCal and Background observations. The Spec2Pipeline was run using default parameters but skipping the CubeBuild and Extract1D steps. The Spec2Pipeline was run on the background exposures,⁶ treating them as science data. Next, association files were generated for combining the four dither positions. The Spec3Pipeline was then called with default parameters but skipping the OutlierDetection and Extract1D steps. The Level-3 spectral cubes were built in the ifualign coordinate system using Shepard’s method with exponential weighting (emsm) for mapping the data into a rectilinear cube. For IRAS 21282+5050-RIM, first, the background exposures were subtracted from the level-2 calibrated science exposures. The JWST Calibration Pipeline version 1.10.0 was used with CRDS context `jwst_1077.pmap` running under Python 3.11.2. It is noted that the calibration reference files and pipeline software are continuously updated, and data fidelity is expected to improve with time, e.g., flux calibration, spike detection, treatment of $1/f$ noise, etc.

Spectral extraction is done on the Level-3 data for each grating/filter combination separately using a $1''.5$ radius circular aperture centered on the field of view, defined as an Astropy Region. Subsequently, the extraction aperture was converted to a pixel-weighted image mask. For each wavelength slice, missing or invalid data overlapping the aperture are linearly interpolated in the spatial domain, where the interpolation aperture is taken as a circle with a radius 3 pixels larger than that of the extraction aperture. The spectrum, in spectral units of MJy sr^{-1} , is computed as the sum of the science data cube multiplied by the image mask resized to match the cube’s spectral axis and multiplied by the ratio of the area per pixel over the area of the aperture. Uncertainties are computed following the same procedure but using the squared error and taking a final square root. In addition, the variation of the extracted signal is recorded as the standard deviation within the extraction aperture, which is a measure of the smoothness across the aperture. Lastly, data quality flags are propagated by `or-ing` all flags within the extraction aperture, where interpolated pixels have bit 7 (RESERVED) set.

The spectra for each grating/filter are combined and written to file in IPAC table format, tabulating wavelength, flux, flux uncertainty, flux variation, order, and flags. At the same time, a header is added that keeps track of pertinent proposal, observation, and reduction parameters using `key/value` pairs. Lastly, the need for stitching is assessed, which was deemed unnecessary.

Spectral extractions focusing on distinct morphological regions and features are planned for forthcoming papers.

3. Results

First, the morphology of the $3.3 \mu\text{m}$ PAH emission for each target is considered. Second, the extracted spectra are explored, taking a closer look at wavelength regions of interest.

3.1. Morphology

Figure 8 presents the $3.29 \mu\text{m}$ slice for each target, i.e., at the peak position of the $3.3 \mu\text{m}$ PAH band. The figure shows that there is well-defined morphological substructure present in most of the images. Notably, the maps of BD +303639-RIM, IRAS 21282+5050-RIM-BKSUB, HD 44179-SPIKE, and NGC 7027-EDGE show that their fields have been aptly labeled RIM, SPIKE, and EDGE. For M17, NGC 1333-SVS3, and NGC 2023-PDR, the substructure is less distinct and more nebulous in nature. Comparison between these maps and the imagery in Section 2 shows good agreement between the substructure observed in both. This is especially true for BD +303639-RIM, IRAS 21282+5050-RIM-BKSUB, and NGC 7027-EDGE but a bit more difficult to discern for both M17 positions, NGC 1333-SVS3, and NGC 2023-PDR, where the field of view is either larger, more crowded, or both. For HD 44179, there appears to be a slight offset between the $3.3 \mu\text{m}$ PAH map and the image that is larger than the $0''.06$ reported rms in R.A. and decl. for the Hubble data. It is noted that the Hubble Legacy Archive offers a number of observations in the same filters having differing coordinate solutions; those used here match the NIRSPEC observations best.

3.2. The Spectra

Figure 9 presents the spectra extracted for each target from their associated $1''.5$ radius circular aperture depicted in Figure 8. The spectra have been presented so as to capture most of their salient features. With the exception of HD 44179-SPIKE, the spectra show a rising continuum with wavelength that steps up around $3.2 \mu\text{m}$. The spectrum of HD 44179-SPIKE is unusual in that the continuum rises up to the $3.3 \mu\text{m}$ PAH band, after which it drops again. Investigating this further revealed that the diffraction spike from a secondary mirror strut is aligned with the leg of the “x” in the NIRSPEC field of view, contaminating the extracted spectrum (T. Keyes 2023, private communication).

All spectra have an easily distinguishable, strong $3.3 \mu\text{m}$ PAH band; a discernible $3.4 \mu\text{m}$ feature; a sharp rise at the onset of the $5.25 \mu\text{m}$ PAH band; and numerous emission lines. Notably, BD +303639-RIM shows a relatively strong forest of emission lines, whereas both M17 positions, NGC 1333-SVS3, NGC 2023-PDR, and NGC 7027-EDGE have a plethora of relatively weaker lines. For IRAS 21282+5050-RIM-BKSUB and HD 44179-SPIKE, the emission lines are more subdued. The spectra of the two M17 positions and NGC 1333-SVS3 show CO_2 -ice absorption around $4.27 \mu\text{m}$ and signs of a very broad H_2O -ice absorption band, most apparent between 2.8 and $3.2 \mu\text{m}$. The spectra of IRAS 21282+5050-RIM, HD 44179-SPIKE, NGC 1333-SVS3, and NGC 7027-EDGE show signs of CO gas emission around $4.66 \mu\text{m}$.

The variation of the spectral signal within the extraction aperture (gray envelopes) differs considerably between the targets. It is most notable for IRAS 21282-RIM and HD 44179-SPIKE and somewhat present for BD +303639-RIM and NGC 7027-EDGE. This is consistent with the morphology of these sources depicted in Figure 8. That is, they either have a strong gradient in surface brightness or a distinct morphological feature within the extraction aperture.

The PAH-related features in the spectra are explored in the next section, followed by the CO_2 -ice absorption band, CO gas, atomic, and molecular emission lines. Besides a direct spectral

⁶ The background of IRAS 21282+5050-RIM caused the pipeline to issue a warning and skip the background-subtraction step.

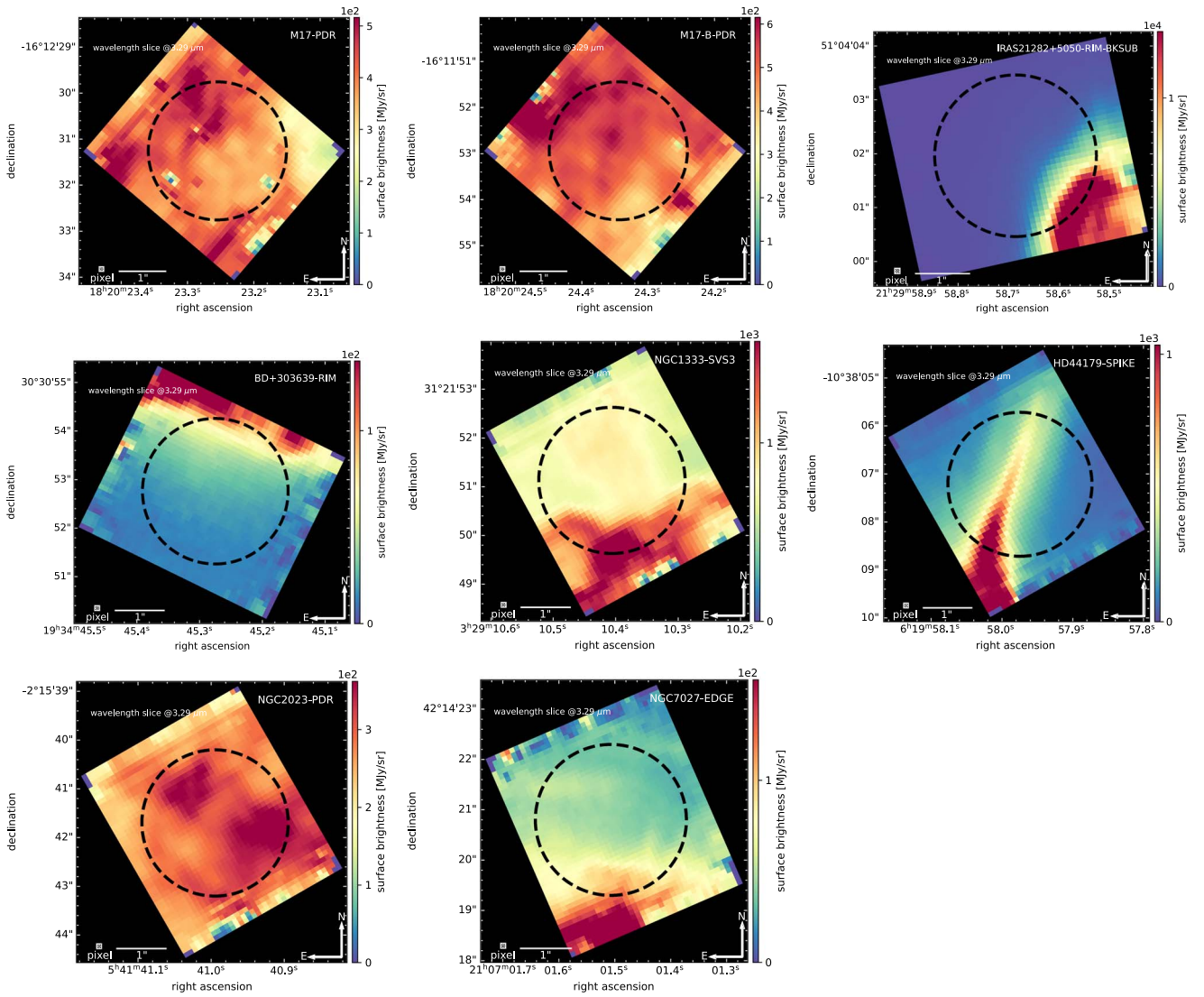


Figure 8. $3.29\ \mu\text{m}$ slices of the NIRSpect-IFU spectral-spatial data cubes. Indicated are the $1.5''$ radius circular extraction apertures (black dashed) used in this work, the $0.1'' \times 0.1''$ pixel size, a $1''$ scale bar, and the directions of north and east.

comparison between targets, some astrophysical analysis is performed to provide a flavor of the kind of information that is contained in the data. Since the spectra have been extracted from a single large aperture that for most targets includes edges, rims, ridges, etc., the analysis is predominantly limited to M17-B-PDR. In-depth spectral-spatial analyses of all features and targets are planned for a series of forthcoming papers, as this is beyond the scope of this first exploratory look.

3.2.1. PAH Spectral Features

PAH-related spectral regions of interest are considered next.

The 3.2–3.6 μm CH stretch region—Figure 10 compares the 3.2–3.6 μm region for each target. To separate the broad PAH-related features from the underlying plateau, a local spline continuum has been subtracted with knots at the fixed wavelength positions of 3.21, 3.37, 3.54, and 3.59 μm (see also Figure 14). Besides the dominant 3.3 μm band with its blue shoulder, distinct, broad features peaking at roughly 3.395, 3.408, 3.465, 3.515, and 3.560 μm are common to all spectra. The 3.3 μm PAH band peaks at 3.29 μm for most targets, with

a few peaking at slightly longer wavelengths due to the H I Pf:9-5 recombination line being superimposed. The relative intensities of the PAH-related features show some variation between objects. The strongest of these, centered at 3.4 μm , is a doublet with separate components at 3.395 and 3.408 μm . The 3.408 and 3.465 μm bands are most prominent in IRAS 21282 +5050-RIM-BKSUB.

The 1.6–1.7 μm CH stretch overtone region—The first overtone of the 3.3 μm PAH band is predicted to fall in this region (Duley 1994; Chen et al. 2019), with a tentative detection reported by Geballe et al. (1994) in IRAS 21282 +5050. Figure 11 zooms in on the 1.6–1.7 μm region for each target. The spectra have been scaled by setting the minimum in the region to zero and the height to half that of the strongest line. Except perhaps for IRAS 21282+5050-RIM-BKSUB, the figure shows that there is little evidence for distinct emission near 1.68 μm that can be directly associated with an overtone of the 3.3 μm PAH band. For IRAS 21282+5050-RIM-BKSUB, a broad undulating “continuum” can be seen that rises and falls from 1.63 to 1.67 μm and rises again from 1.67 to longward of 1.7 μm .

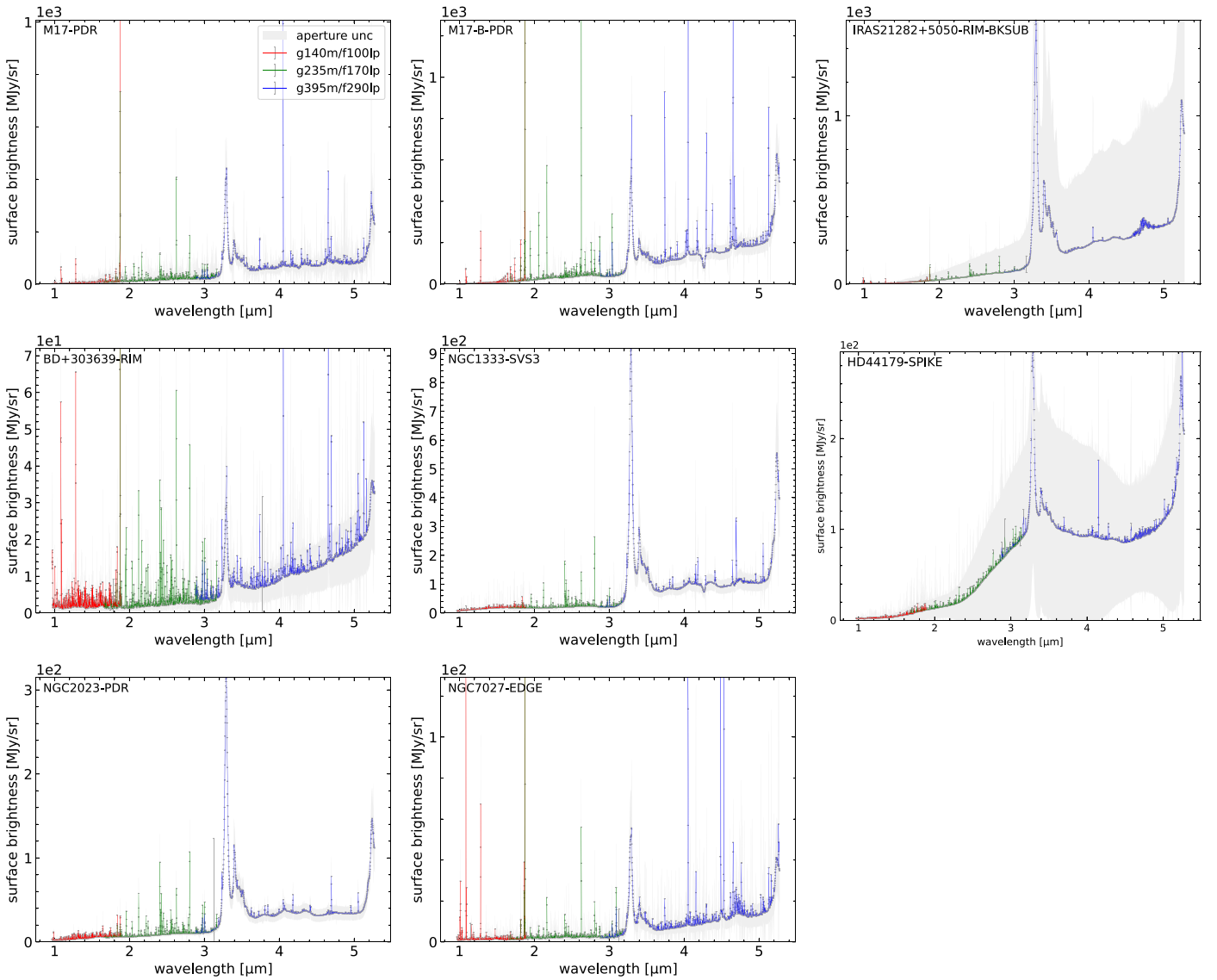


Figure 9. NIRSpc-IFU 1–5 μm spectra for each target extracted from a $1''.5$ radius circular aperture. Each grating/filter combination has been color-coded, and 1σ error bars are indicated (darker gray), which are typically smaller than the line width. The envelopes (gray) show the 1σ variation of the spectral signal within the extraction aperture.

The 4.3–4.8 μm deuterated and PAH nitrile region—Figure 12 compares the 4.3–4.8 μm region for each target, indicating where emission features from deuterated and PAH nitriles have been predicted to fall (e.g., Buragohain et al. 2020; Allamandola et al. 2021, and references therein). For the figure, each spectrum has been continuum subtracted using a spline with anchor points at 4.30, 4.45, 4.60, and 4.78 μm and is offset. Except for NGC 7027-EDGE, this removes the continuum adequately, leaving only a small amount of residual broadband structure in a few spectra.

Any clear detection of the aliphatic CD stretch at 4.65 μm is severely hampered by CO emission in the spectra of HD 44179-SPIKE, IRAS 21282+5050-RIM-BKSUB, NGC 1333-SVS3, and NGC 7027-EDGE. For M17-PDR, M17-B-PDR, and NGC 1333-SVS3, such a feature could be hidden in the broad blended emission complex apparent in their spectra. The remaining spectra show no clear evidence for this feature. Similarly, the aromatic CD band centered around 4.4 μm is also confused by line emission.

Following the approach by Doney et al. (2016), the left panel of Figure 13 decomposes the 4.60–4.72 μm spectrum of M17-B-PDR into multiple components by simultaneously fitting a first-order polynomial baseline, six narrow Gaussian profiles to match the emission lines, and one broad Gaussian representing emission that may be attributable to the aliphatic CD stretch. A feature is recovered at $4.649 \pm 0.001 \mu\text{m}$, consistent with the astronomical position reported by Doney et al. (2016). The feature has an integrated intensity of $2.73 \pm 0.52 \times 10^{-21} \text{ W cm}^{-2}$ and a signal-to-noise ratio of 5.25.

Likewise, the right panel of Figure 13 decomposes the 4.35–4.45 μm spectrum of M17-B-PDR using a similar approach to search for emission attributable to the aromatic CD stretch. However, there is no compelling evidence for such a feature (signal-to-noise ratio of 0.39).

Combining the deuterated PAH intensities with the values determined for the 3.3 μm aromatic CH stretch and 3.4 μm aliphatic CH stretch bands in M17-B-PDR of $7.28 \pm 0.493 \times 10^{-20}$ and $7.53 \pm 1.48 \times 10^{-21} \text{ W cm}^{-2}$, respectively, yields $I_{4.4}/I_{3.3} = 4.94 \pm 12.83 \times 10^{-4}$ and $I_{4.65}/I_{3.4} = 0.36 \pm 0.100$.

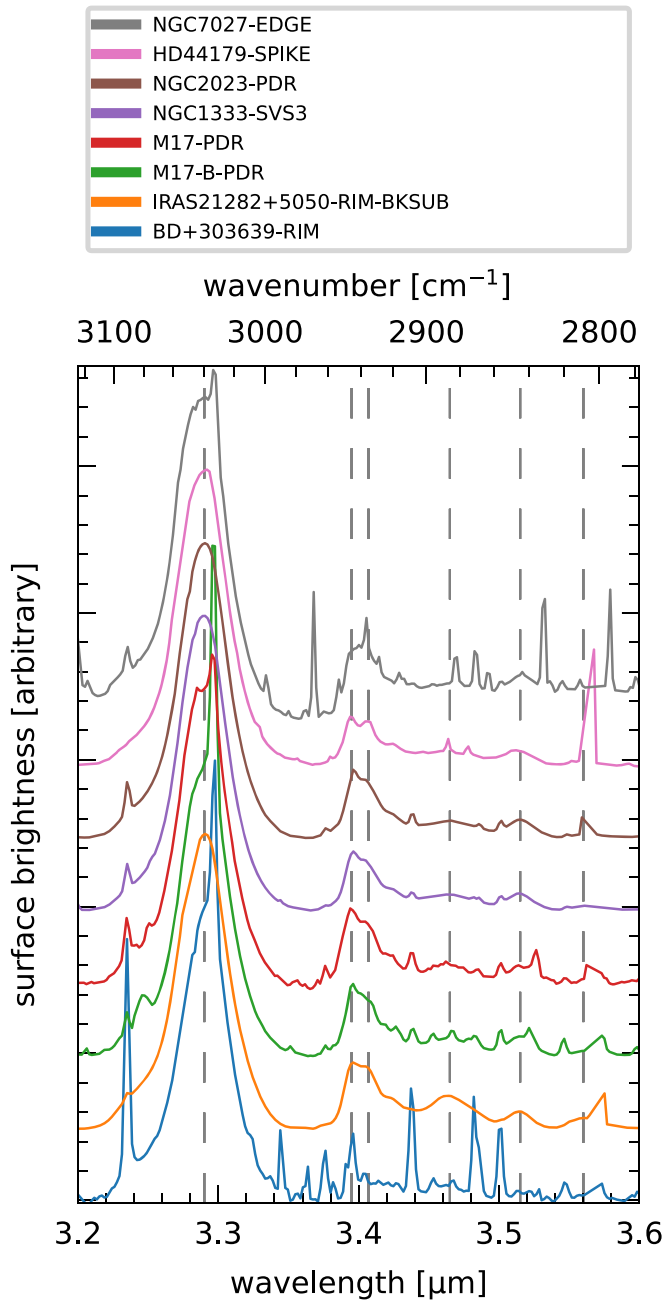


Figure 10. 3.2–3.6 μm region for each target, continuum subtracted, normalized to the peak strength of the 3.3 μm PAH feature, and offset. The gray dashed lines indicate the positions of the broad PAH-related features. See Section 4.1.1 for a discussion.

Then, for simplicity, assuming that the integrated cross sections for the corresponding aromatic and aliphatic C-H/C-D modes are comparable (Peeters et al. 2004) and following Yang et al. (2020), the degree of deuteration can be estimated. Here the ratio of integrated cross sections $A_{4.40}/A_{3.3} = 0.56 \pm 0.19$, and the blackbody intensity ratio $B(3.3)/B(4.4) = 0.70 \pm 0.28$ ($400 \text{ K} \lesssim T_{\text{PAH}} \lesssim 900 \text{ K}$). With the observed ratio $I_{4.4}/I_{3.3}$, the degree of aromatic deuteration $[D/H]_{\text{arom.}} = 0.06\% \pm 0.16\%$. Similarly, with the observed aliphatic ratio $I_{4.65}/I_{3.4}$, $[D/H]_{\text{alip.}} = 31\% \pm 12.7\%$ for M17-B-PDR.

The 1–5 μm PAH continuum—Figure 14 indicates what is dubbed here the PAH continuum (initially called the “vibrational quasi-continuum”; Allamandola et al. 1989). The 1–5 μm portion starts near 1.2 μm and rises slowly to

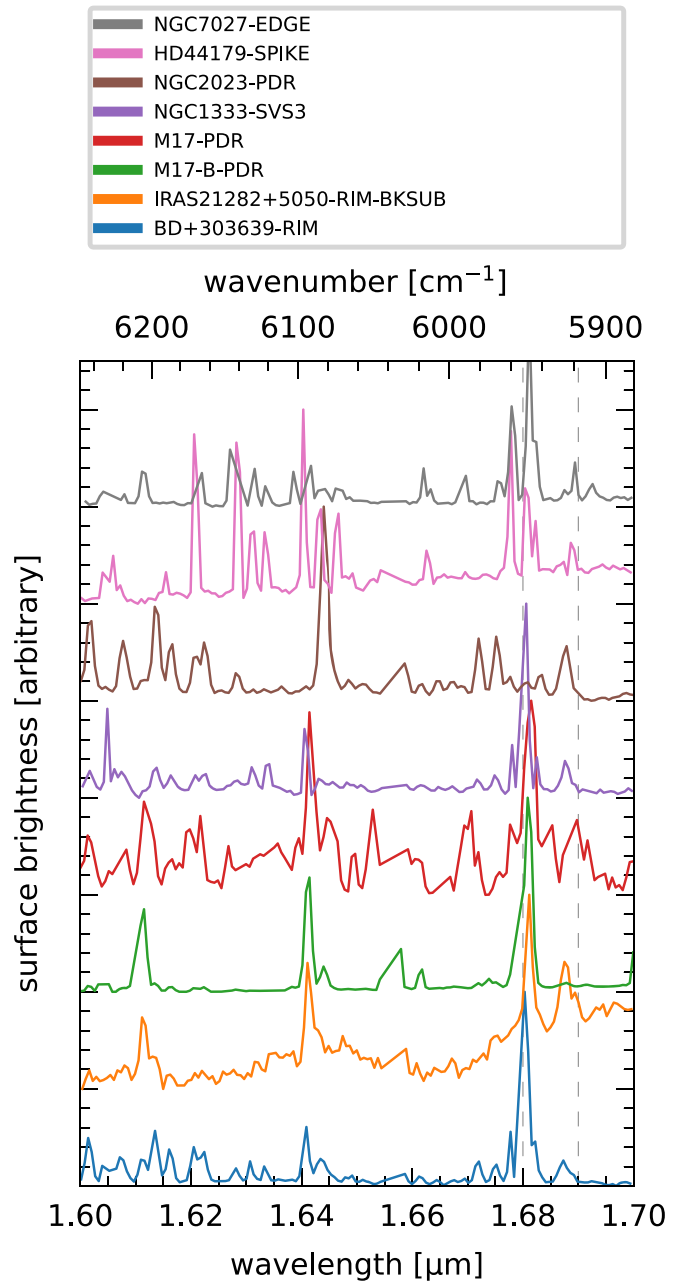


Figure 11. 1.6–1.7 μm region for each target, scaled and offset. The gray dashed lines bracket the nominal position of the $\nu = 2-0$ overtone of the 3.3 μm PAH band. It is noted that the triangle-like structure seen between ~ 1.655 and $1.659 \mu\text{m}$ is the result of an incomplete removal of a data spike. See Section 4.1.2 for a discussion.

$\sim 3.2 \mu\text{m}$, where it steps up by a factor of ~ 2.5 , after which it stays relatively flat out to $5 \mu\text{m}$. This step-up is distinct from the emission underlying the 3.3/3.4 μm PAH band complex indicated in the figure. Broad bumps that are part of this continuum are centered near 3.8, 4.04, and 4.34 μm and can be seen in all targets but BD +303639+RIM and NGC 7027-EDGE, where they are possibly hidden by the forest of intense emission lines.

3.2.2. $\text{CO}_2/\text{H}_2\text{O}$ -ice Absorption, CO Gas, and Line Emission

The spectra in Figure 9 show signs of CO_2 - and H_2O -ice absorption bands, gas-phase CO rovibrational lines, and atomic and molecular line emission, which are considered next.

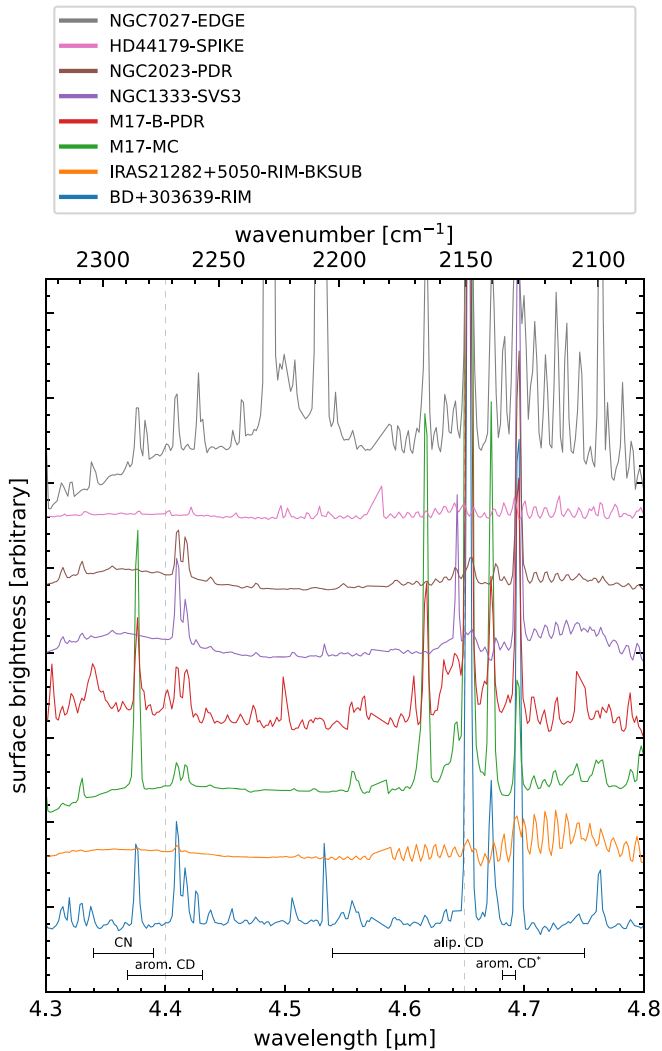


Figure 12. 4.3–4.8 μm region for each target, continuum subtracted and offset. Indicated are predicted regions where the aromatic and aliphatic CD stretches and the CN stretch in PAH nitriles fall (Bauschlicher et al. 1997; Hudgins et al. 2004; Allamandola et al. 2021; Esposito et al. 2023, in preparation). The gray dashed lines indicate their typical astronomical positions. Range found for the aromatic CD stretch in pentacene. See Section 4.1.3 for a discussion.

The 4.2–4.3 μm CO_2 - and 2.8–3.2 μm H_2O -ice absorption bands—The left panel of Figure 15 compares the 4.2 μm CO_2 -ice absorption signatures detected at both M17 positions and NGC 1333-SVS3. A spline with anchor points near 4.200, 4.318, and 4.350 μm has been used to determine the optical depth of each of the CO_2 -ice features. The figure shows quite some variation, with maximum optical depths of ~ 0.6 , 0.3, and 0.1 for M17-B-PDR, M17-PDR, and NGC 1333-SVS3, respectively.

Utilizing the absorption data for an $\text{H}_2\text{O}+\text{CO}_2$ (10:1) ice at 10 K from the Leiden Ice Database (Ehrenfreund et al. 1999; Rocha et al. 2022), Figure 16 shows the result of a simultaneous fit to the 4.20–4.35 μm spectrum of M17-B-PDR with a first-order polynomial baseline, four Gaussian profiles for the emission lines, and attenuation by absorption of the CO_2 water ice. This produces a good match, yielding a column density of $10.0 \pm 0.30 \times 10^{17} \text{ cm}^{-2}$ for the ice.

Lastly, the very broad and strong H_2O -ice absorption band falling between 2.8 and 3.2 μm is observed in the spectra of M17-PDR, M17-B-PDR, and NGC 1333-SVS3 (see Figure 9).

However, its analysis is more challenging due to the overlap with the 3.3 μm PAH complex.

The 4.6–4.9 μm CO gas emission lines—The right panel of Figure 15 compares the rovibrational structure of CO gas emission that is apparent in the spectra of IRAS 21282+5050-RIM-BKSUB, HD 44179-SPIKE, NGC 1333-SVS3, and NGC 7027-EDGE. Here a local spline continuum with anchor points at 4.400, 4.500, 4.605, 4.900, and 4.995 μm is first subtracted from each spectrum, after which it is scaled to emphasize the rovibrational structure.

Figure 17 simultaneously fits the 4.50–4.85 μm spectrum of IRAS 21282+5050-RIM-BKSUB with a third-order polynomial, Gaussian emission lines at 4.65 and 4.70 μm , and a simple rigid-rotor CO model with power and temperature as free parameters. The fit is very reasonable, especially given the simplicity of the employed CO model, and indicates warm CO gas at a temperature of $T_{\text{CO}} = 258 \pm 17 \text{ K}$.

Emission lines—The spectra in Figure 9 show a plethora of emission lines spread across the entire 1–5 μm region. To generate an inventory, an uncurated list of some 17,000 lines between 0.6 and 5.3 μm is considered. This list contains transition data for atomic Al, Ar, C, Ca, Co, Fe, He, H I, K, Mg, N, Ni, O, and P and molecular H_2 and HD. Here the line lists for H_2 from Roueff et al. (2019) and HD from HITRAN (Rothman 2021) are combined with atomic data from the Atomic Line List⁷ (v3.00b4; van Hoof 2018). Each line is blindly fitted to the spectrum per grating/filter combination in $\lambda-F_\lambda$ space using a Gaussian line profile together with a first-order polynomial baseline. The fit is performed across the wavelength range made up of 14 adjacent resolution elements around the line center, allowing for up to $\pm 10^{-4} \mu\text{m}$ variation in the line position and a minimum and maximum FWHM of 0.001 and 0.02 μm , respectively. Power and line width are forced strictly positive. Line strength, propagated uncertainty, and contrast are determined from each fit, where lines with a signal-to-noise ratio greater than 2, a contrast above 5%, and an integrated intensity of at least $10^{-23} \text{ W cm}^{-2}$ are recorded.

Figure 18 presents the results for M17-B-PDR, where 1002 lines from a total of seven species have been matched. Still, a number of unmatched lines remain. There is clearly a considerable amount of line confusion. That is, there are only 198 lines that are spaced more than $5 \times 10^{-3} \mu\text{m}$ apart. This confusion is driven by an enormous number of closely spaced He and HD lines and not applying any priors based on the astrophysical environment to down-select the line list. For example, the matches of high-energy lines such as [Ar VI] and [Ca VIII] are hard to reconcile with the astrophysical environment of M17-B-PDR. Similarly, the presence of cobalt is highly unlikely given its low cosmic abundance and that no matching lines were found for other metals, e.g., iron.

H I lines—Further demonstrating the richness and fidelity of the line data, Figure 19 zooms in on the atomic hydrogen Pfund series, starting from an upper level of 10 to well into the 30s. These lines can be, e.g., a powerful diagnostic for the geometry of the source (Lenorzer et al. 2002).

H I recombination lines can be used to determine the extinction along the line of sight (Gurzadyan 1997). For example, considering the $\text{Br}\beta$ and $\text{Br}\alpha$ lines at 2.63 and 4.05 μm , respectively, and Case B recombination (Baker & Menzel 1938), the total visual extinction A_V can be deduced

⁷ www.pa.uky.edu/~peter/newpage/index.html

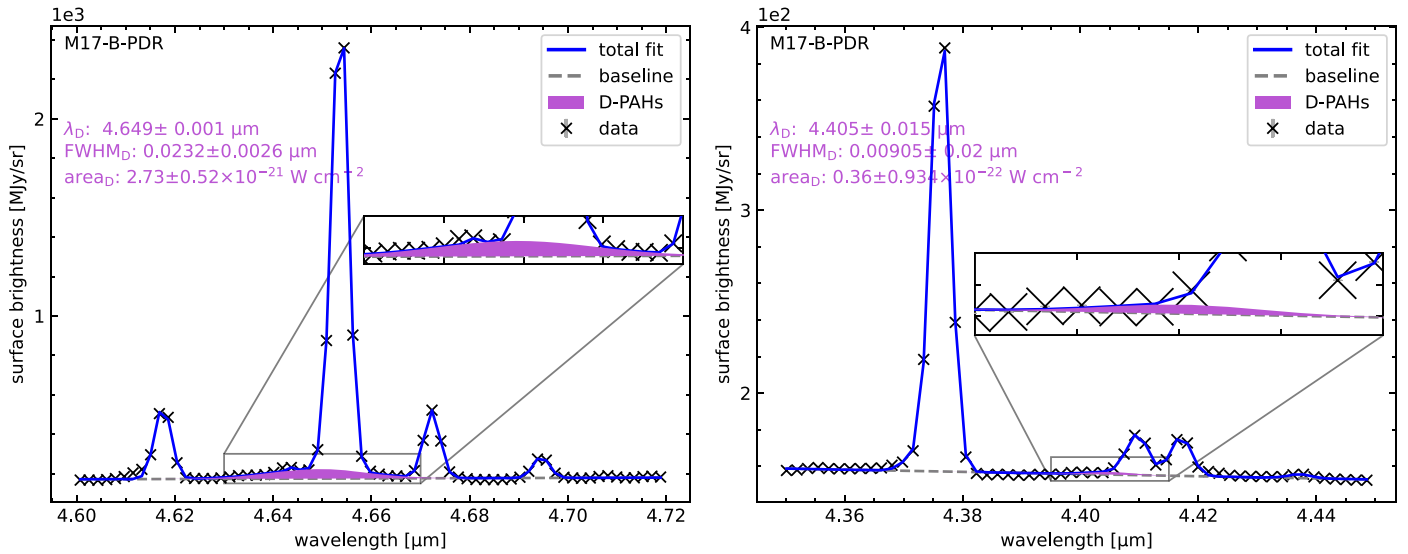


Figure 13. Zoom-in and multicomponent decomposition of the 4.60–4.72 (aliphatic region; left) and 4.33–4.47 (aromatic region; right) μm spectra of M17-B-PDR. The properties of the component possibly attributable to deuterated PAHs (purple) are given. See Section 4.1.3 for a discussion.

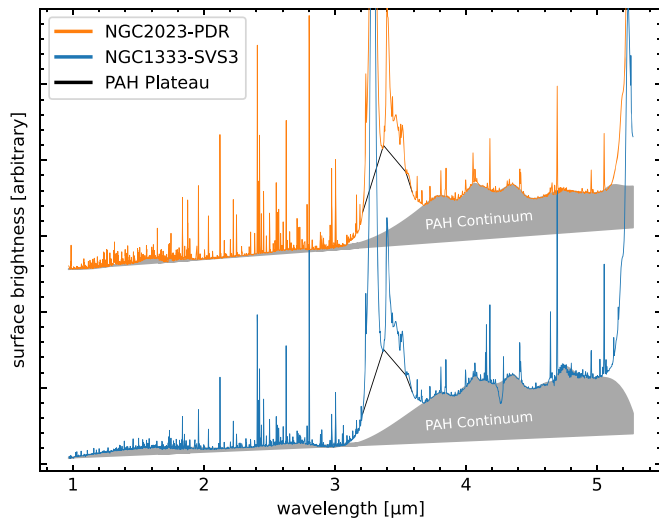


Figure 14. 1–5 μm spectra of NGC 2023-PDR and NGC 1333-SVS3 indicating the PAH continuum (dark gray). The triangular shaped region below the 3.3/3.4 μm band complex (black line segments) designates emission associated with the 3 μm band complex. See Section 4.1.4 for a discussion.

from

$$\frac{I(\text{Br}\beta)}{I(\text{Br}\alpha)} = \left[\frac{I(\text{Br}\beta)}{I(\text{Br}\alpha)} \right]^* 10^{0.4A_V \frac{N_{\text{H}}}{A_V} (C_{\text{ext}}(\text{Br}\alpha) - C_{\text{ext}}(\text{Br}\beta))}, \quad (1)$$

where $I(\text{Br}\beta)/I(\text{Br}\alpha) = 0.381 \pm 0.01966$ is the attenuated line ratio measured from the NIRSpc spectrum of M17-B-PDR, $[I(\text{Br}\beta)/I(\text{Br}\alpha)]^* = 0.572$ is the no-extinction value from Storey & Hummer (1995), $A_V/N_{\text{H}} = 5.3 \times 10^{-22} \text{ cm}^2$ is taken from Weingartner & Draine (2001), and the extinction cross sections $C_{\text{ext}}(\text{Br}\alpha) = 2.816$ and $C_{\text{ext}}(\text{Br}\beta) = 5.694 \times 10^{-23} \text{ cm}^2 \text{ H}^{-1}$ when using the $R_V = 5.5$ curve from Weingartner & Draine (2001).⁸ Furthermore, $[I(\text{Br}\beta)/I(\text{Br}\alpha)]^*$ is computed assuming

⁸ $R_V = 5.5$ is chosen, as it provides the most consistent results when performing spectral decomposition on the Spitzer spectral cube of M17 (Boersma et al. 2018) and is somewhat in line with Chini & Wargau (1998), who found $R_V = 4.8$.

an electron temperature of $T_e = 10^4 \text{ K}$ and an electron density of $n_e = 3 \times 10^3 \text{ cm}^{-3}$. This exercise results in a considerable total visual extinction of $A_V \simeq 8$, which is agreeable with that found by Glushkov et al. (2005) and Boersma et al. (2018).

H₂ lines—Pure, $v = 0-0$, rotational H_2 lines can be used to derive the molecular hydrogen column density and gas temperature from fits to population diagrams such as that presented in Figure 20 (e.g., Fleming et al. 2010; Boersma et al. 2018). A straight-line fit to the (not extinction-corrected) log-linear data in Figure 20, simultaneously optimizing the ortho-to-para ratio (R_{OP}), gives a column density of $N_{\text{H}_2} = 6.0 \pm 0.5 \times 10^{15} \text{ cm}^{-2}$, hot $T_{\text{H}_2} = 2239 \pm 34 \text{ K}$ gas, and an ortho-to-para ratio of $R_{\text{OP}} = 2.86 \pm 0.04$.

4. Discussion

All targets display a spectrum with a rich and varying inventory of features that, taken together, help paint an astrophysical picture of the targeted areas. That is, each of the spectral components reveals something distinct about the astronomical environment. For example, the PAH bands provide direct insight into the level of excitation induced by the radiation field and the chemical complexity that is present. Similarly, ice absorption bands give an impression of the molecular diversity encountered along the line of sight, and the atomic and molecular emission lines reveal gas densities and temperatures. Furthermore, the spectra probe distinct extended regions with different and changing morphologies spanning the aperture at unprecedented spatial resolution. Moreover, each target represents a different stage along the stellar life cycle, from star formation to stellar death. This changing astrophysical environment is reflected by the spectra through the appearance and disappearance of features, variations in relative intensities, the shape of the continuum, and band profiles.

What follows is a discussion of the PAH-related bands and other spectral features. The focus will be predominantly on the former, as studying PAHs and PAH-related emission is the main objective of JWST GO Cycle 1 program 1591. Density functional theory (DFT)-computed PAH spectra that take anharmonicity into account are relied upon to provide a

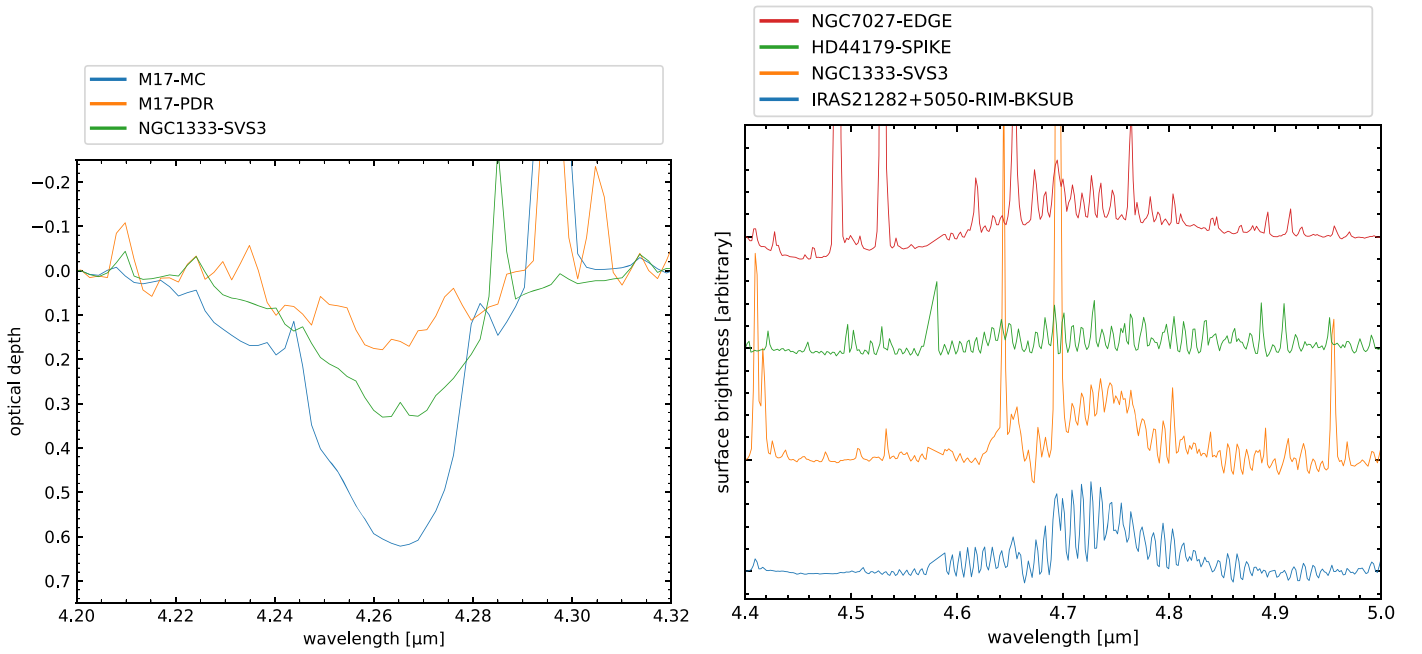


Figure 15. Comparison of the observed 4.2 μm CO_2 -ice absorption (left) and CO rovibrational emission (right). See Sections 4.2 and 4.3 for discussions.

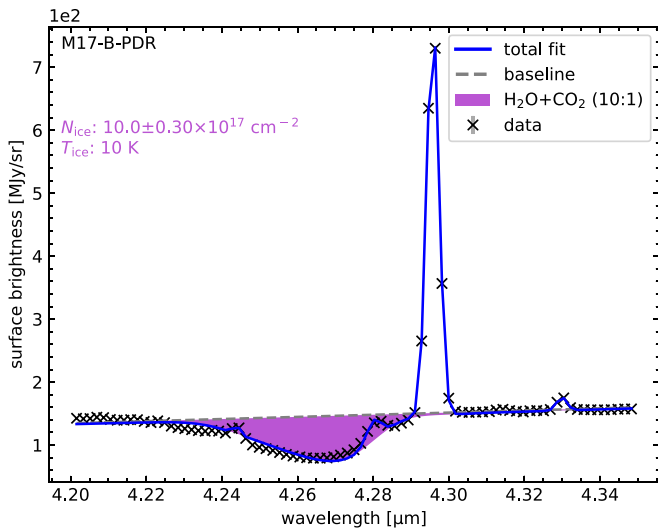


Figure 16. Multicomponent fit of the CO_2 -ice absorption band in the spectrum of M17-B-PDR. The purple shaded area indicates the $\text{H}_2\text{O}:\text{CO}_2$ (10:1) 10 K ice component. See Section 4.2 for a discussion.

backbone for the interpretation. Much of the discussion will be centered on the results obtained for M17-B-PDR in Section 3.2.

4.1. PAH Emission

The familiar PAH emission bands between 3 and 20 μm originate from PAH fundamental transitions, such as CH and CC stretches and bends, emitting from the first vibrational level, i.e., $v = 1-0$. While the only PAH fundamentals that fall in the 1–5 μm range are the strong aromatic and aliphatic CH stretching bands that dominate the 3.2–3.5 μm region, other, weaker PAH emission features fill the entire 1–5 μm range producing the PAH continuum (e.g., Allamandola et al. 1989, 2021; Esposito et al. 2023).

These weaker features are attributed to the effects of anharmonicity, where vibrationally excited PAHs relax from

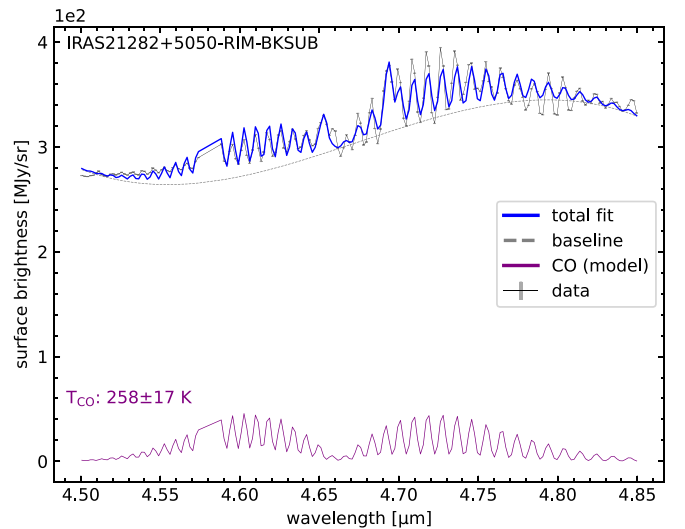


Figure 17. Warm, 258 K, CO gas detected in emission in the spectrum of IRAS 21282+5050-RIM-BKSUB. Note that the flat-appearing structure around 4.58 μm is due to a spike in the data being masked. See Section 4.3 for a discussion.

higher vibrational levels by emitting (1) directly to the ground state, (2) stepwise down the vibrational ladder, and (3) in combination with other vibrational modes (i.e., $\nu_{\text{CC}} + \nu_{\text{CH}}$). In addition, signatures of deuterated and PAH nitriles also fall in this wavelength range (e.g., Allamandola et al. 1989, 2021).

DFT computations are utilized to aid in the interpretation of the PAH emission in the NIRSpec data. Previously, PAH spectra have been predominantly computed using the harmonic approximation for frequencies and the double harmonic approximation for intensities. This approach has shortcomings in predicting band positions and strengths for higher vibrational states that fall in and dominate the 1–5 μm region. With JWST now providing unprecedented high-fidelity coverage of this wavelength range, commensurate theoretical methods that intrinsically include some level of anharmonicity are required.

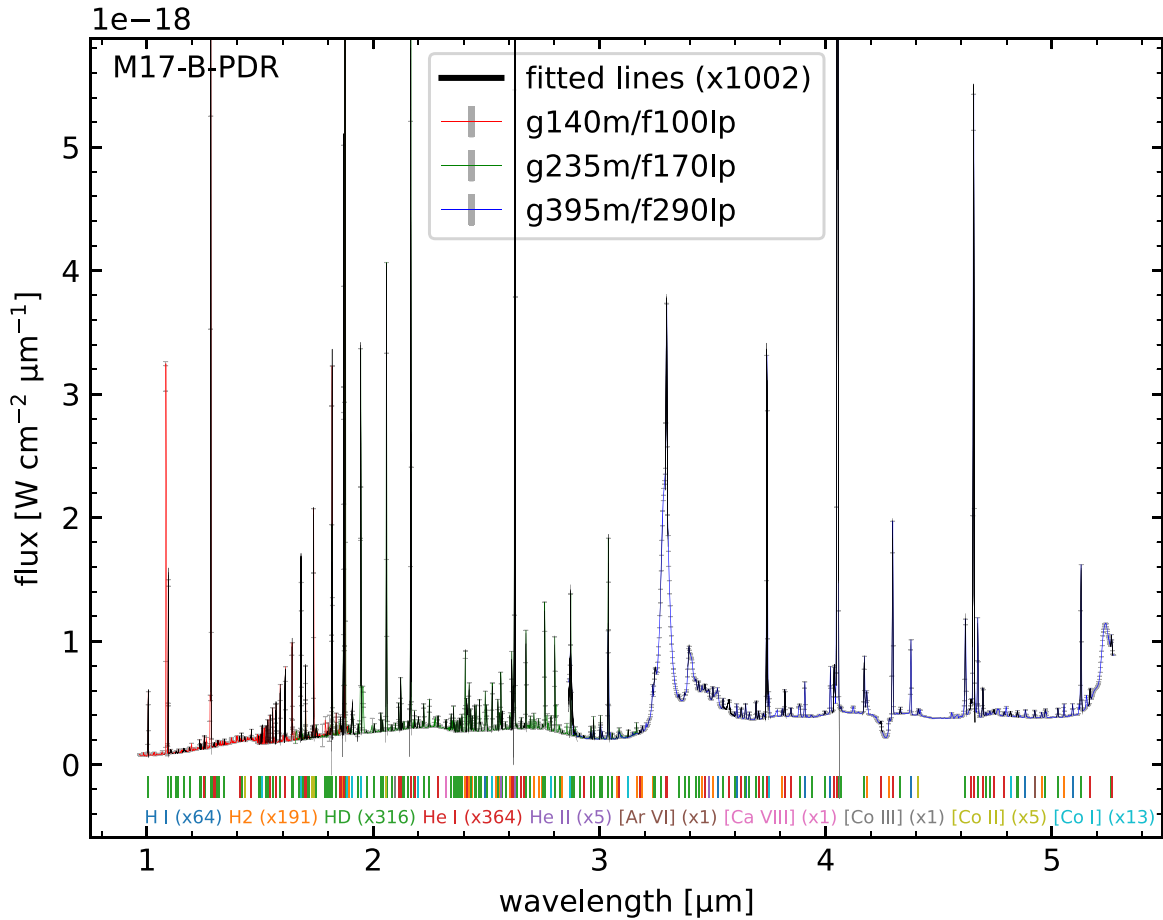


Figure 18. Line analysis of M17-MC, given a line list of some 17,000 lines results in 1002 matches. Only lines with a signal-to-noise ratio of at least 2, a contrast of 5%, and an integrated intensity of at least 10^{-23} W cm^{-2} are shown. Each species/ionization state has been color-coded separately. The number of lines matched per species is provided in parentheses. Note that not all lines are matched, and there are those that are simultaneously matched by several species. Only 198 lines are spaced apart more than 5×10^{-3} μm .

Until recently, those methods could not be applied to molecules as large as PAHs. That has changed thanks to the development of novel techniques and the increase in computational power (Mackie et al. 2015, 2016, 2018, 2022; Chen et al. 2019). To that end, Esposito et al. (2023) carried out DFT computations utilizing the Gaussian 16 quantum chemistry package (Frisch et al. 2016) with the B3LYP method in conjunction with the N07D (Barone & Cimino 2008; Barone et al. 2010) basis set in order to obtain 1–30 μm anharmonic absorption spectra for phenanthrene, pyrene, and pentacene. Also, new computations were performed that include unique singly substituted, deuterated isotopologues, as well as singly substituted cyano (nitrile) side groups (V. J. Esposito et al. 2023, in preparation).

4.1.1. The 3.2–3.6 μm CH Stretching Region

The 3.2–3.6 μm region is dominated by the strong aromatic CH stretching fundamental band at 3.3 μm and the moderately intense complex of overlapping bands between ~ 3.38 and 3.6 μm that are associated with aliphatic CH stretching modes and combination band and overtone transitions from longer-wavelength PAH modes (e.g., Barker et al. 1987; Joblin et al. 1995; Pech et al. 2002; Maltseva et al. 2015; Mackie et al. 2022).

The prominent 3.3 μm band originates from the aromatic CH stretch in relatively smaller, neutral PAHs (Allamandola et al.

1999). Its profile and width were characterized by van Dienenhoven et al. (2004) into classes A, B1, and B2. Here the bands peaking at 3.290, 3.293, and 3.297 μm are associated with classes A, B1, and B2, respectively. For most astronomical PAH sources, the band is symmetric and of class A with an FWHM of ~ 0.04 μm . Class B sources are less common and have an FWHM of ~ 0.037 μm . In a number of cases, as also seen in some of the NIRSpec spectra presented here, the band is crowned with the Pfd emission line at 3.296 μm . Emission around 3.3 μm is highly sensitive to anharmonicity and Fermi resonances (Mackie et al. 2015, 2018, 2022), which can express themselves as substructure in the band profile, e.g., its blue shoulder or satellite features at ~ 3.4 –3.6 μm , and/or contribute to the plateau-like emission underlying the discrete band.

The distinct feature at 3.4 μm , besides being in part due to PAH anharmonicity, has been attributed to aliphatics, e.g., suprahydrogenated PAHs. Post-AGB sources with extremely large 3.3/3.4 μm band ratios have an accompanying 6.9 μm band attributed to the methylene scissoring mode (e.g., Materese et al. 2017). Furthermore, the smooth evolution of the peak position of the PAH bands as a function of the effective temperature of the radiation field has been interpreted as a transition to a more aromatic nature of the emitting materials, i.e., the loss of aliphatic side groups (Bregman & Temi 2005; Sloan et al. 2007). Here the NIRSpec data show a

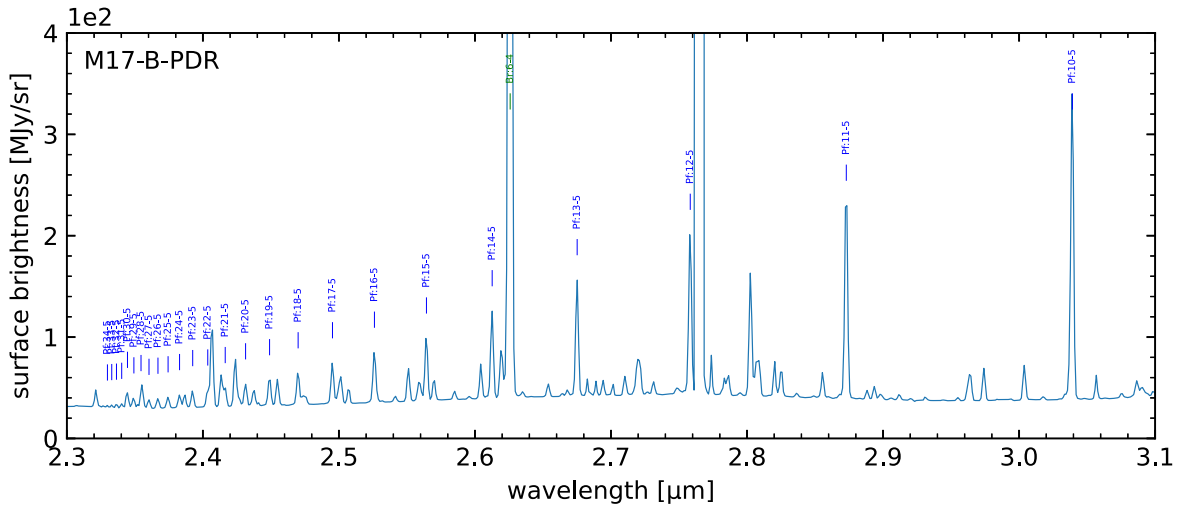


Figure 19. The 2.3–3.1 μm spectrum of M17-B-PDR depicting a rich inventory of H I emission lines, notably the Pfund series, where each transition has been labeled separately.

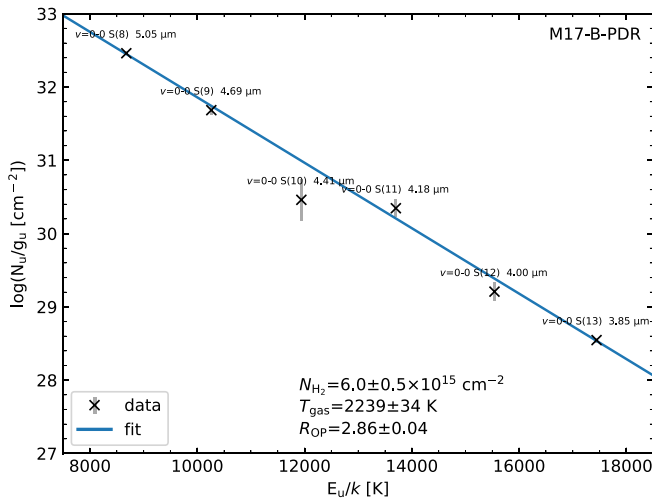


Figure 20. Pure rotational (not extinction-corrected) H_2 $v=0-0$ population diagram analysis of the spectrum of M17-B-PDR. The propagated statistical uncertainties have been indicated. The blue line shows the best fit, with the derived parameters given, including their uncertainties. See Section 3.2.2 for details and Section 4.3 for a discussion.

more typical astronomical 3.4 μm band, suggesting that these sources are well inside the aromatic domain. This is also consistent with extremely large 3.4/3.3 μm band ratios and a smooth evolution of peak position with effective temperature mainly being observed for class C sources, which are mostly evolved stars (e.g., Geballe et al. 1992; Goto et al. 2007; Sloan et al. 2007).

4.1.2. The 1.6–1.7 μm CH Stretch Overtone Region

A number of astronomical studies have searched for the $v=2-0$ overtone transition of the 3.3 μm band, which, on first principles, is expected to fall near ~ 1.67 μm (Magazzu & Strazzulla 1992; Siebenmorgen & Peletier 1993; Geballe et al. 1994). A tentative detection was reported by Geballe et al. (1994) in IRAS 21282+5050. However, as Figure 11 reveals, any detection in the NIRSspec spectra can be heavily confused with strong emission lines.

Chen et al. (2019) showed, based on anharmonic DFT computations for eight PAHs in the C_{14} – C_{20} size range, that

PAH combination bands fall between 1.63 and 1.67 μm and pile up between 1.65 and 1.66 μm . However, overtones of the aromatic CH stretches are weak and rare. This is consistent with the results for phenanthrene, pyrene, and pentacene found here, where the first overtones of the aromatic CH stretches fall between 1.62 and 1.66 μm (6173 – 6024 cm^{-1}), while significantly stronger combination bands with one CH stretch quanta and one other high-intensity mode quanta are spread across the 1.6–1.7 μm (6260 – 5882 cm^{-1}) range. The CN and CD first overtones, however, are predicted at longer wavelengths.

Thus, on top of strong line confusion, any signal that can be isolated from the NIRSspec data and associated with PAHs cannot be directly attributed solely to the $v=2-0$ overtone of the 3.3 μm band.

4.1.3. The 4.3–4.8 μm Deuterated and PAH Nitrile Region

Deuterated PAHs—A wide range in the D/H gas ratio has been observed across the Galaxy (e.g., Friedman et al. 2023). One possible explanation for this variation is the depletion of D onto PAHs via H exchange reactions in UV-rich environments (e.g., Draine 2004). As D is more strongly bound to a PAH than H, with the passage of time, D enrichment builds, potentially leading to substantial PAH D/H ratios (e.g., Peeters et al. 2004; Onaka et al. 2014, 2022; Doney et al. 2016).

Previous laboratory and harmonic DFT computational studies undertaken to determine the band positions of the CD stretches showed that the aromatic stretches fall near 4.40 μm , and the aliphatic CD stretches fall near 4.65 μm . However, these positions shift slightly depending on the PAH edge structure, extent of deuteration, and charge (Bauschlicher et al. 1997; Hudgins et al. 2004). Many have searched for these signatures in astronomical data, with some reporting success (e.g., Hudgins et al. 2004; Peeters et al. 2004; Doney et al. 2016; Yang et al. 2020; Onaka et al. 2022). However, the predicted band positions of deuterated PAHs coincide with strong emission lines from atoms and molecules, and, before JWST, observations were severely hampered by poor signal-to-noise ratios and/or limited spectral resolution.

New anharmonic DFT computations to help identify signatures from deuterated PAHs in the NIRSspec data consider all of the unique singly substituted, deuterated isotopologues for phenanthrene, pyrene, and pentacene (Esposito et al. 2023,

in preparation). For phenanthrene and pyrene, the aromatic CD stretch fundamental transitions are predicted to fall between 4.36 and 4.43 μm (2290 and 2130 cm^{-1}), in line with Hudgins et al. (2004). However, for pentacene, the aromatic CD stretches fall between 4.68 and 4.69 μm .

PAH nitriles—The recent discoveries of radio emission from benzonitrile ($\text{C}_6\text{H}_5\text{-C}\equiv\text{N}$), two cyanonaphthalenes (1- $\text{C}_{10}\text{H}_7\text{-C}\equiv\text{N}$ and 2- $\text{C}_{10}\text{H}_7\text{-C}\equiv\text{N}$), and other small aromatic species containing $\text{C}\equiv\text{N}$ in TMC-1 and, recently, other cold clouds (McGuire et al. 2018, 2021; Agundez et al. 2023) suggest that cyano-PAHs (nitriles) could be an important subset of the astronomical PAH family.

Allamandola et al. (2021) reported the CN stretch fundamental transitions of benzonitrile and other smaller, nonaromatic nitriles as falling between 4.46 and 4.5 μm . New anharmonic computations of the CN stretch fundamental transitions for all unique isomers of singly substituted cyano-benz[a]anthracene have a different range of 4.34–4.39 μm (2300–2275 cm^{-1} ; Esposito et al. 2023, in preparation). This is narrower than and overlaps with the wavelength range for many deuterated PAHs (4.36–4.43 μm). For completeness, new harmonic DFT computations of the CN stretch for all unique isomers of singly substituted large PAHs containing between 35 and 45 carbon atoms are consistent with the 4.34–4.39 μm range. Figure 12 indicates that there is no clear-cut feature attributable to CN in this range.

Thus, given the limited range for the position of the computed CN stretch fundamental, any new feature observed between 4.36 and 4.69 μm that lies outside 4.34–4.39 μm may be due to the CD stretch fundamental transition.

Summing up, inspection of Figure 12 shows that despite huge improvements in spectral capabilities, the NIRSpec data do not allow for a straightforward assignment of any feature to deuterated and/or PAH nitriles. A decomposition method has to be employed to deal with the still-present line confusion. For M17-B-PDR, this resulted in a potential feature at 4.65 μm that could be attributable to the aliphatic CD stretch in deuterated PAHs, but, in agreement with Peeters et al. (2004), the absence of any reliable detection of a feature around 4.40 μm in M17 that could be attributed to the aromatic CD stretch is curious.

The [D/H] ratio determined for M17-B-PDR from the NIRSpec data based on the aliphatic content alone matches that reported by Peeters et al. (2004; 0.31 ± 0.127 versus 0.36 ± 0.08). However, this ratio is expected to depend on the exact location of the nebula probed and the employed (emission) model (Onaka et al. 2014; Doney et al. 2016).

4.1.4. The 1–5 μm PAH Continuum

Upon absorption of a UV photon, all PAH fundamental modes are temporarily vibrationally excited to some extent as the excitation energy is distributed and redistributed across the molecule during the relaxation process. The main relaxation channel is through the stepwise emission of infrared photons at frequencies corresponding to their fundamental vibrational frequencies, as well as combinations and overtones of those frequencies. The emission from this very large number of PAH transitions produces a continuum that spans the near-, mid-, and most of the far-infrared (e.g., Allamandola et al. 1989, 2021; Esposito et al. 2023, and references therein). The first astronomical reporting of such a continuum was by Sellgren (1984).

PAHs containing some 40–70 carbon atoms, typical for the astronomical PAH population, have roughly 180–240 fundamental vibrational modes and thousands of combination band and overtone transitions. The density of these states for PAHs containing 40 carbon atoms is approximately 1×10^{23} states cm^{-1} at 1 μm and 1×10^7 states cm^{-1} at 5 μm . For a 70 carbon atom sized PAH, these are 1×10^{31} states cm^{-1} at 1 μm and 1×10^{10} states cm^{-1} at 5 μm . High vibrational excitation of PAHs lowers the symmetry of the molecule. During absorption from the ground state, symmetry-defined vibrational selection rules are rigid. In the case of emission, where the transition begins in a vibrationally excited state, previously symmetry-forbidden transitions (to infrared dark states) become weakly allowed. Thus, apart from expecting the intensity of each overtone band to drop as it progresses to higher-order overtones, due to a decrease in the intrinsic intensity of the participating vibrational transitions, it is impossible to predict their relative intensities a priori (Herzberg 1945).

The 1–5 μm part of the PAH continuum is largely ascribed to first-order combination bands and overtones of the strong PAH fundamental bands in the 5–15 μm region. Likewise, while dominated by the familiar PAH spectral signatures, the 5–15 μm region itself includes PAH continuum emission from similar combination bands of the many longer-wavelength, low-frequency PAH fundamentals described in Ricca et al. (2010) and Boersma et al. (2011). Although significantly weaker than the strong fundamentals, blended emission from these contribute to the 5–15 μm region. This process continues into the far-infrared, with emission from combination bands of even longer-wavelength bands continuously contributing to the emission at shorter wavelengths until the density of states drops such that continuum emission breaks up and falls away around 100 μm (Ricca et al. 2010; Boersma et al. 2011).

Although visible in earlier observations (e.g., Draine 2001; Ohsawa 2016), NIRSpec now allows for the full characterization of the 1–5 μm continuum component of the astronomical PAH emission spectrum, revealing three broad bumps centered near 3.8, 4.04, and 4.34 μm whose positions suggest they could arise from combinations and overtones of the familiar 7.7, 7.8, and 8.6 μm PAH bands.

4.2. Ices

The absorption by cold CO_2 water ice in both M17 spectra and that of NGC 1333-SVS3, likely with other ice bands as well (e.g., H_2O), will be spatially separated from the carriers of the other spectral components. As the low temperature of the CO_2 ice in M17-B-PDR suggests, the ices are likely associated with cold foreground molecular cloud material in the line of sight. In this specific case, it appears that the light from the bright background PDR is making it partially through the foreground molecular material, in places being attenuated by denser filaments and cores.

The ices provide sites for ongoing chemistry, i.e., factories for creating more complex organic molecules like PAHs with aliphatic side groups (e.g., Bouwman et al. 2011; Cook et al. 2015). When eventually released as the PDR eats further and further into the molecular cloud material, this could help maintain any aliphatic fraction to support some 3.4 μm emission.

Ices will (partially) obscure any emission feature with which there is a spectral overlap. Thus, special care needs to be taken

in the analysis and interpretation of such features. This includes features in the NIRSpec range but also beyond, at mid-infrared wavelengths, including the major PAH bands. One specific example is CO-ice absorption at $4.67\ \mu\text{m}$ obscuring potential emission from D and/or PAH nitriles at $4.65\ \mu\text{m}$ (Onaka et al. 2022).

4.3. Atomic and Molecular Lines

The rich inventory of atomic and molecular lines found in the NIRSpec spectra offers many diagnostic capabilities, e.g., photon or shock heating, and provide probes for the physical conditions of the gas, including its kinematics, cooling, and chemistry (van Dishoeck 2004; Wolfire et al. 2022).

The warm CO gas detected in IRAS 21282+5050-RIM-BKSUB is likely associated with the PDR and consistent with detection at other wavelengths here and in other evolved stars (Meixner et al. 1993; Davis et al. 2003). The resolved fundamental P-R branch emission from CO would partially overlap with any potential deuterated and/or cyano-PAH bands at $4.65\ \mu\text{m}$. Thus, separating such emission from the CO rovibrational structure and other confused lines requires care.

In the case of molecular hydrogen, collisions keep the lowest rotational levels of ($v=0$, $J<5$) in thermal equilibrium and thus provide a good indicator of the gas temperature and insight into the ortho-to-para ratio (e.g., Sternberg 1989; Habart et al. 2005). However, the population diagram in Figure 20 probes the $J>5$ S(8)–S(13) lines. Thus, the levels in the NIRSpec range are excited through UV pumping (Habart et al. 2005), which is further confirmed by the 1–0 S(1)/2–1 S(1) ratio of 2.0 (see, e.g., Burton et al. 2002). Furthermore, in equilibrium, the ortho-to-para ratio R_{OP} is expected to be 3, with 2.86 found here for M17-B-PDR. Therefore, the high temperature for M17-B-PDR needs to be interpreted as an excitation temperature.

4.4. Variations along the Stellar Life Cycle

Along the stellar life cycle, gas and dust flow through ever-changing environments of varying densities, temperatures, and radiation fields. Some environments will promote an increase in chemical complexity, be it through gas-phase reactions or grain surface chemistry, while others will reduce chemical complexity, and only the most robust chemical species and particles survive.

Besides reflecting the current astrophysical environment, infrared spectra also capture the history of the gas and dust. The NIRSpec spectra presented here sample a number of key stages along the low-mass stellar life cycle. Although similar overall, there are a number of striking and subtle differences. With the emphasis on PAH and related features, PAHs are not only silent witnesses of local conditions, they also help shape their environment. It is this interplay that simultaneously reveals characteristics of the PAH population itself and the astrophysical environment in which they reside (e.g., Tielens 2008).

5. Summary and Conclusions

JWST represents a giant leap in infrared spectral–spatial fidelity and sensitivity. A first look at the 1–5 μm observations from JWST GO Cycle 1 program 1591 has been presented here. Using NIRSpec-IFU, the program targets seven objects along the low-mass stellar life cycle with PAH emission.

Aperture positions were chosen such that they capture a varying morphology with gradients, ridges, and distinct features, which allows for a spatial analysis across single extended objects. Some of the spectra show notable variation within their extraction aperture. These variations are consistent with the spatial morphology that can be observed in their 3.3 μm PAH maps and line up well with what is seen in color composite imagery that reveals the overall larger-scale structure of the targeted regions.

This first look paper explores the spectrum of each target extracted from a $1''.5$ radius circular aperture centered on the field of view. All spectra show a wealth of features, including the 3.3 and 3.4 μm PAH complex, the PAH continuum, and a vast array of atomic and molecular emission lines, including H I, H₂, and likely an array of other species. Some spectra also show absorption by CO₂ and H₂O ice and emission from warm gas-phase CO.

For most sources, the prominent PAH CH stretch band is symmetric and of class A, peaking at $3.29\ \mu\text{m}$ (FWHM = $0.04\ \mu\text{m}$). Its anticipated $v=2-0$ overtone at $1.68\ \mu\text{m}$ is confused by line emission in all targets. The 3.4 μm band shows two varying components that can be ascribed to aliphatic CH stretches and/or hot bands of the aromatic CH stretch.

The PAH continuum, characterized for the first time, spans most of the 1–5 μm region. Rising slowly from $\sim 1\ \mu\text{m}$, it jumps near $3.2\ \mu\text{m}$ and slowly continues to rise out to $5\ \mu\text{m}$. Broad bumps at roughly 3.8, 4.04, and $4.34\ \mu\text{m}$ add structure for all but the spectra of NGC 7027-EDGE and BD +303639-RIM, where they could be hidden by the forest of emission lines.

Despite JWST’s spectral resolution and sensitivity, identifying possible emission from deuterated and/or cyano-PAHs remains challenging. For the bright-PDR position in M17, a multicomponent decomposition was carried out. While this indeed suggests that an aliphatic CD stretch feature centered at $4.65\ \mu\text{m}$ (FWHM = $0.02\ \mu\text{m}$) is present, consistent with earlier work, there is no hint of the aromatic CD stretch at $4.40\ \mu\text{m}$. The latter is also true for any cyano-PAH feature between 4.34 and $4.39\ \mu\text{m}$. Thus, despite huge improvements in spectral resolution and sensitivity, at this stage of analysis, these NIRSpec spectra do not allow for a straightforward assignment of any feature due to deuterated and/or cyano-PAHs.

The CO₂ absorption band seen in the M17-B-PDR spectrum is well matched with 10:1 H₂O:CO₂ ice at 10 K. A two-component fit to its $v=0$ pure rotational molecular hydrogen population diagram shows high-temperature gas that, given the high- J rotational lines, originates from UV-pumped gas. M17-B-PDR also shows a large number of hydrogen recombination lines, with the atomic hydrogen Pfund series running from level 10 to well into the 30s. Considering $\text{Br}\beta/\text{Br}\alpha = 0.382 \pm 0.2002$ and Case B recombination, an estimated total visual extinction of $A_V \simeq 8$ is found for M17-B-PDR.

Lastly, the rovibrational structure of CO seen in the spectrum of IRAS 21282+5050 is well matched with warm, 258 K, gas.

6. Software and Third-party Data Repository Citations

The JWST data presented in this paper were obtained from the Mikulski Archive for Space Telescopes (MAST) at the Space Telescope Science Institute (STScI). The STScI-reduced observations can be accessed via [10.17909/x16g-g718](https://doi.org/10.17909/x16g-g718). The STScI is operated by the Association of Universities for

Research in Astronomy, Inc., under NASA contract NAS526555. Support to MAST for these data is provided by the NASA Office of Space Science via grant NAG57584 and by other grants and contracts.

Where indicated, color composite images were created from observations made with the NASA/ESA Hubble Space Telescope. Those data were obtained from the Hubble Legacy Archive, which is a collaboration between the Space Telescope Science Institute (STScI/NASA), the Space Telescope European Coordinating Facility (ST-ECF/ESA), and the Canadian Astronomy Data Centre (CADC/NRC/CSA).

Density functional theory computations were performed using the Gaussian 16 software suite (Frisch et al. 2016).

Acknowledgments

This work would not have been possible without T.J.L., who passed away during the development of this project. His guiding hand and expertise in computational chemistry as applied to astronomy and astrophysics will be deeply missed by this team and all in the community.

This project is based on observations made with JWST. Financial support from the Space Science Telescope Institute is acknowledged (GO-01591). C.B. is grateful for an appointment at NASA Ames Research Center through the San José State University Research Foundation (80NSSC22M0107). C.B., J. D.B., L.J.A., and A.M. acknowledge support from the Internal Scientist Funding Model (ISFM) Laboratory Astrophysics Directed Work Package at NASA Ames (22-A22ISFM-0009). L.J.A., J.D.B., and A.M. are thankful for an appointment at NASA Ames Research Center through the Bay Area Environmental Research Institute (80NSSC19M0193). V.J.E.'s research has been supported by an appointment to the NASA Postdoctoral Program at NASA Ames Research Center, administered by the Oak Ridge Associated Universities through a contract with NASA. R.C.F. is grateful for support from NASA grants NNX17AH15G and NNX22ZHA004C, the University of Mississippi's College of Liberal Arts, and the Mississippi Center for Supercomputing Research, which is funded in part by NSF grant OIA-1757220. E.P. acknowledges support from the University of Western Ontario, the Institute for Earth and Space Exploration, the Canadian Space Agency, and the Natural Sciences and Engineering Research Council of Canada. Special thanks go to program coordinator W. J. Skipper, NIRSpec reviewer K. Namisha, and the JWST Help Desk, notably T. Keyes, for technical support. Lastly, the anonymous referee is gratefully acknowledged for the valuable insight and feedback.

Facility: JWST(NIRSpec).

Software: Astropy (Astropy Collaboration et al. 2013, 2018), JWST Calibration Pipeline (Bushouse et al. 2023).

ORCID iDs

C. Boersma  <https://orcid.org/0000-0002-4836-217X>
 L. J. Allamandola  <https://orcid.org/0000-0002-6049-4079>
 V. J. Esposito  <https://orcid.org/0000-0001-6035-3869>
 A. Maragkoudakis  <https://orcid.org/0000-0003-2552-3871>
 J. D. Bregman  <https://orcid.org/0000-0002-1440-5362>
 P. Temi  <https://orcid.org/0000-0002-8341-342X>
 T. J. Lee  <https://orcid.org/0000-0002-2598-2237>
 R. C. Fortenberry  <https://orcid.org/0000-0003-4716-8225>
 E. Peeters  <https://orcid.org/0000-0002-2541-1602>

References

- Abergel, A., Bernard, J. P., Boulanger, F., et al. 2001, *A&A*, **389**, 239
 Agundez, M., Marcelino, N., Tercero, B., & Cernicharo, J. 2023, *A&A*, **677**, L13
 Allamandola, L. J., Boersma, C., Lee, T. J., Bregman, J. D., & Temi, P. 2021, *ApJL*, **917**, L35
 Allamandola, L. J., Hudgins, D. M., & Sandford, S. A. 1999, *ApJL*, **511**, L115
 Allamandola, L. J., Tielens, A. G. G. M., & Barker, J. R. 1989, *ApJS*, **71**, 733
 Andrews, H., Boersma, C., Werner, M. W., et al. 2015, *ApJ*, **807**, 99
 Astropy Collaboration, Price-Whelan, A. M., Sipőcz, B. M., et al. 2018, *AJ*, **156**, 123
 Astropy Collaboration, Robitaille, T. P., Tollerud, E. J., et al. 2013, *A&A*, **558**, A33
 Baker, J. G., & Menzel, D. H. 1938, *ApJ*, **88**, 52
 Barker, J. R., Allamandola, L. J., & Tielens, A. G. G. M. 1987, *ApJL*, **315**, L61
 Barone, V., Bloino, J., & Biczysko, M. 2010, *PCCP*, **12**, 1092
 Barone, V., & Cimino, P. 2008, *CPL*, **454**, 139
 Bauschlicher, C. W., Langhoff, S. R., Sandford, S. A., & Hudgins, D. M. 1997, *JPCA*, **101**, 2414
 Beintema, D. A., van den Ancker, M. E., Molster, F. J., et al. 1996, *A&A*, **315**, L369
 Bernard-Salas, J., Pottasch, S. R., Wesselius, P. R., & Feibelman, W. A. 2003, *A&A*, **406**, 165
 Boersma, C., Bauschlicher, C. W., Jr., Ricca, A., et al. 2011, *ApJ*, **729**, 64
 Boersma, C., Bregman, J., & Allamandola, L. J. 2016, *ApJ*, **832**, 51
 Boersma, C., Bregman, J., & Allamandola, L. J. 2018, *ApJ*, **858**, 67
 Böker, T., Arribas, S., Lützgendorf, N., et al. 2022, *A&A*, **661**, A82
 Böker, T., Beck, T. L., Birkmann, S. M., et al. 2023, *PASP*, **135**, 038001
 Bouwman, J., Mattioda, A. L., Linnartz, H., & Allamandola, L. J. 2011, *A&A*, **525**, A93
 Bregman, J., & Temi, P. 2005, *A&A*, **621**, 831
 Bregman, J. D., Booth, J., Gilmore, D. K., Kay, L., & Rank, D. 1992, *ApJ*, **396**, 120
 Buragohain, M., Pathak, A., Sakon, I., & Onaka, T. 2020, *ApJ*, **892**, 11
 Burton, M. G., Londish, D., & Brand, P. W. J. L. 2002, *MNRAS*, **333**, 721
 Bushouse, H., Eisenhamer, J., Dencheva, N., et al. 2023, JWST Calibration Pipeline (1.10.0) Zenodo, doi:10.5281/zenodo.7795697
 Candian, A., Kerr, T. H., Song, I. O., McCombie, J., & Sarre, P. J. 2012, *MNRAS*, **426**, 389
 Chen, T., Luo, Y., & Li, A. 2019, *A&A*, **632**, A71
 Chini, R., Elsaesser, H., & Neckel, T. 1980, *A&A*, **91**, 186
 Chini, R., & Wargau, W. F. 1998, *A&A*, **329**, 161
 Cohen, M., & Jones, B. F. 1987, *ApJL*, **321**, L151
 Cook, A. M., Ricca, A., Mattioda, A. L., et al. 2015, *ApJ*, **799**, 14
 Cox, P. 1998, *Ap&SS*, **255**, 489
 Crete, E., Giard, M., Joblin, C., et al. 1999, in *ESA SP-427, The Universe as Seen by ISO*, ed. P. Cox & M. Kessler (Noordwijk: ESA), 663
 Dalton, G. B., Caldwell, M., Ward, A. K., et al. 2006, *Proc. SPIE*, **6269**, 0
 Davis, C. J., Smith, M. D., Stern, L., Kerr, T. H., & Chiar, J. E. 2003, *MNRAS*, **344**, 262
 de Graauw, T., Haser, L. N., Beintema, D. A., et al. 1996, *A&A*, **315**, L49
 Doney, K. D., Candian, A., Mori, T., Onaka, T., & Tielens, A. G. G. M. 2016, *A&A*, **586**, A65
 Draine, B. 2004, in *Origin and Evolution of the Elements*, ed. A. McWilliam & M. Rauch (Cambridge: Cambridge Univ. Press)
 Draine, B. T., & Li, Aigen 2001, *ApJ*, **551**, 807
 Duley, W. W. 1994, *ApJL*, **429**, L91
 Ehrenfreund, P., Kerkhof, O., Schutte, W. A., et al. 1999, *A&A*, **350**, 240
 Emerson, J., McPherson, A., & Sutherland, W. 2006, *Msngr*, **126**, 41
 Esposito, V. J., Allamandola, L. J., Boersma, C., et al. 2023, *MolPh*, **0**, e2252936
 Fleming, B., France, K., Lupu, R. E., & McCandliss, S. R. 2010, *ApJ*, **725**, 159
 Friedman, S. D., Chayer, P., Jenkins, E. B., et al. 2023, *ApJ*, **946**, 34
 Frisch, M. J., Trucks, G. W., Schlegel, H. B., et al., 2016 *Gaussian 16 Revision C.02*, (Wallingford, CT: Gaussian Inc)
 Gaia Collaboration 2020, *VizieR Online Data Catalog*, I/350
 Gardner, J. P., Mather, J. C., Abbott, R., et al. 2023, *PASP*, **135**, 068001
 Geballe, T. R., Joblin, C., D'Hendecourt, L. B., et al. 1994, *ApJL*, **434**, L15
 Geballe, T. R., Tielens, A. G. G. M., Kwok, S., & Hrivnak, B. J. 1992, *ApJL*, **387**, L89
 Glushkov, Y. I., Esipov, V. F., & Kondrat'eva, L. N. 2005, *ARep*, **49**, 36
 Goto, M., Kwok, S., Takami, H., et al. 2007, *ApJ*, **662**, 389
 Gurzadyan, G. A. 1997, *The Physics and Dynamics of Planetary Nebulae* (Berlin: Springer), 53
 Habart, E., Walmsley, M., Verstraete, L., et al. 2005, *SSRv*, **119**, 71

- Herzberg, G. 1945, *Molecular Spectra and Molecular Structure II. IR and Raman Spectroscopy of Polyatomic Molecules* (Toronto: D. Van Nostrand Company)
- Hsia, C.-H., Zhang, Y., Kwok, S., & Chau, W. 2019, *Ap&SS*, **364**, 32
- Hudgins, D. M., Bauschlicher, C. W., Jr., & Sandford, S. A. 2004, *ApJ*, **614**, 770
- Jiang, Z., Yao, Y., Yang, J., et al. 2002, *ApJ*, **577**, 245
- Joblin, C., Boissel, P., Leger, A., D'Hendecourt, L., & Defourneau, D. 1995, *A&A*, **299**, 835
- Joblin, C., Tielens, A. G. G. M., Geballe, T. R., & Wooden, D. H. 1996, *ApJL*, **460**, L119
- Kharchenko, N. V., Piskunov, A. E., Röser, S., Schilbach, E., & Scholz, R.-D. 2005, *A&A*, **438**, 1163
- Kwok, S., Hrivnak, B. J., & Langill, P. P. 1993, *ApJ*, **408**, 586
- Latter, W. B., Dayal, A., Biegging, J. H., et al. 2000, *ApJ*, **539**, 783
- Lenorzer, A., de Koter, A., & Waters, L. B. F. M. 2002, *A&A*, **386**, L5
- Leuhenagen, U., Hamann, W.-R., & Jeffery, C. S. 1996, *A&A*, **312**, 167
- Mackie, C. J., Candian, A., Huang, X., et al. 2015, *JChPh*, **143**, 224314
- Mackie, C. J., Candian, A., Huang, X., et al. 2016, *JChPh*, **145**, 084313
- Mackie, C. J., Candian, A., Lee, T. J., & Tielens, A. G. G. M. 2022, *JPCA*, **126**, 3198
- Mackie, C. J., Chen, T., Candian, A., Lee, T. J., & Tielens, A. G. G. M. 2018, *JChPh*, **149**, 134302
- Magazu, A., & Strazzulla, G. 1992, *A&A*, **263**, 281
- Maltseva, E., Petrigiani, A., Candian, A., et al. 2015, *ApJ*, **814**, 23
- Materese, C. K., Bregman, J. D., & Sandford, S. A. 2017, *ApJ*, **850**, 165
- McGuire, B. A., Burkhardt, A. M., Kalenskii, S., et al. 2018, *Sci*, **359**, 202
- McGuire, B. A., Loomis, R. A., Burkhardt, A. M., et al. 2021, *Sci*, **371**, 1265
- Meixner, M., Skinner, C. J., Temi, P., et al. 1993, *ApJ*, **411**, 266
- Menten, K. M., Reid, M. J., Forbrich, J., & Brunthaler, A. 2007, *A&A*, **474**, 515
- Mookerjee, B., Sandell, G., Jarrett, T. H., & McMullin, J. P. 2009, *A&A*, **507**, 1485
- Moutou, C., Verstraete, L., Sellgren, K., & Leger, A. 1999, in *ESA Special Publication, Vol. 427, The Universe as Seen by ISO*, ed. P. Cox & M. Kessler (ESA), 727
- Nagashima, C., Nagayama, T., Nakajima, Y., et al. 1999, in *Star Formation 1999*, ed. T. Nakamoto (Nagano: Nobeyama Radio Observatory), 397
- Ohsawa, Ryou, Onaka, Takashi, Sakon, Itsuki, Matsuura, Mikako, & Kaneda, Hidehiro 2016, *AJ*, **151**, 93
- Onaka, T., Matsuhara, H., Wada, T., et al. 2007, *PASJ*, **59**, S401
- Onaka, T., Mori, T. I., Sakon, I., et al. 2014, *ApJ*, **780**, 114
- Onaka, T., Sakon, I., & Shimonishi, T. 2022, *ApJ*, **941**, 190
- Pech, C., Joblin, C., & Boissel, P. 2002, *A&A*, **388**, 639
- Peeters, E., Allamandola, L. J., Bauschlicher, C. W., Jr., et al. 2004, *ApJ*, **604**, 252
- Peeters, E., Bauschlicher, C. W., Jr., Allamandola, L. J., et al. 2017, *ApJ*, **836**, 198
- Peeters, E., Tielens, A. G. G. M., Allamandola, L. J., & Wolfire, M. G. 2012, *ApJ*, **747**, 44
- Persi, P., Cesarsky, D., Marenzi, A. R., et al. 1999, *A&A*, **351**, 201
- Pilleri, P., Montillaud, J., Berné, O., & Joblin, C. 2012, *A&A*, **542**, A69
- Povich, M. S., Churchwell, E., Biegging, J. H., et al. 2009, *ApJ*, **696**, 1278
- Racine, R., & van den Bergh, S. 1970, in *IAU Symp. 38, The Spiral Structure of our Galaxy*, ed. W. Becker & G. I. Kontopoulos (Dordrecht: Reidel), 219
- Ricca, A., Bauschlicher, C. W., Mattioda, A. L., Boersma, C., & Allamandola, L. J. 2010, *ApJ*, **709**, 42
- Rocha, W. R. M., Rachid, M. G., Olsthoorn, B., et al. 2022, *A&A*, **668**, A63
- Rothman, L. S. 2021, *NatRP*, **3**, 302
- Roueff, E., Abgrall, H., Czachorowski, P., et al. 2019, *A&A*, **630**, A58
- Sellgren, K. 1984, *ApJ*, **277**, 623
- Sidhu, A., Peeters, E., Cami, J., & Knight, C. 2021, *MNRAS*, **500**, 177
- Siebenmorgen, R., & Peletier, R. F. 1993, *A&A*, **279**, L45
- Siebenmorgen, R., Zijlstra, A. A., & Krügel, E. 1994, *MNRAS*, **271**, 449
- Sloan, G. C., Hayward, T. L., Allamandola, L. J., et al. 1999, *ApJL*, **513**, L65
- Sloan, G. C., Jura, M., Duley, W. W., et al. 2007, *ApJ*, **664**, 1144
- Smith, E. C., Logsdon, S. E., McLean, I. S., et al. 2020, *ApJ*, **902**, 118
- Song, I.-O., Kerr, T. H., McCombie, J., & Sarre, P. J. 2003, *MNRAS*, **346**, L1
- Song, I.-O., McCombie, J., Kerr, T. H., & Sarre, P. J. 2007, *MNRAS*, **380**, 979
- Sternberg, A. 1989, in *Infrared Spectroscopy in Astronomy*, ed. E. Böhm-Vitense (Noordwijk: ESA), 269
- Stock, D. J., Choi, W. D.-Y., Moya, L. G. V., et al. 2016, *ApJ*, **819**, 65
- Storey, P. J., & Hummer, D. G. 1995, *MNRAS*, **272**, 41
- Straizys, V., Corbally, C. J., Kazlauskas, A., & Černis, K. 2002, *BaltA*, **11**, 261
- Tielens, A. G. G. M. 2008, *ARA&A*, **45**, 289
- Tokunaga, A. T., Bernstein, L. S., & Connelley, M. 2022, *ApJ*, **939**, 86
- van Diedenhoven, B., Peeters, E., Van Kerckhoven, C., et al. 2004, *ApJ*, **611**, 928
- van Dishoeck, E. F. 2004, *ARA&A*, **42**, 119
- van Hoof, P. A. M. 2018, *Galax*, **6**, 63
- Verstraete, L., Puget, J. L., Falgarone, E., et al. 1996, *A&A*, **315**, L337
- Walawender, J., Bally, J., Francesco, J. D., Jørgensen, J., & Getman, K. 2008, in *Handbook of Star Forming Regions, Vol. I: The Northern Sky*, ed. B. Reipurth, Vol. 4 (San Francisco, CA: ASP), 346
- Waters, L. B. F. M., Cami, J., de Jong, T., et al. 1998, *Nat*, **391**, 868
- Weingartner, J. C., & Draine, B. T. 2001, *ApJ*, **548**, 296
- Witt, A. N., Vijh, U. P., Hobbs, L. M., et al. 2009, *ApJ*, **693**, 1946
- Wolfire, M. G., Vallini, L., & Chevance, M. 2022, *ARA&A*, **60**, 247
- Yang, X. J., Li, A., & Glaser, R. 2020, *ApJS*, **251**, 12
- Zang, R. X., Peeters, E., & Boersma, C. 2019, *ApJ*, **887**, 46